NASA TECHNICAL REPORT

NASA TR R-182

NASA TR R-182

REYNOLDS NUMBER EFFECTS ON THE INDUCED PRESSURES OF CYLINDRICAL BODIES WITH DIFFERENT NOSE SHAPES AND NOSE DRAG COEFFICIENTS IN HELIUM AT A MACH NUMBER OF 24

by Richard D. Wagner, Jr., and Ralph Watson
Langley Research Center
Langley Station, Hampton, Va.

NATIONAL AERONAUTICS AND SPACE ADMINISTRATION • WASHINGTON, D. C. • NOVEMBER 1963

TECHNICAL REPORT R-182

REYNOLDS NUMBER EFFECTS ON THE INDUCED PRESSURES OF CYLINDRICAL BODIES WITH DIFFERENT NOSE SHAPES AND NOSE DRAG COEFFICIENTS IN HELIUM AT A MACH NUMBER OF 24

By Richard D. Wagner, Jr., and Ralph Watson

Langley Research Center
Langley Station, Hampton, Va.

NATIONAL AERONAUTICS AND SPACE ADMINISTRATION

ERRATA

NASA Technical Report R-182

REYNOLDS NUMBER EFFECTS ON THE INDUCED PRESSURES OF CYLINDRICAL BODIES WITH DIFFERENT NOSE SHAPES AND NOSE DRAG COEFFICIENTS IN HELIUM AT A MACH NUMBER OF 24

By Richard D. Wagner, Jr., and Ralph Watson

November 1963

Page 3, line 19: Change the formula following the definition of $\bar{x}$

from $\frac{M^3\sqrt{C}}{R_x}$ to $M^3\sqrt{\frac{C}{R_x}}$.

Page 24, line 6: The parameter $\frac{M_s{}^3\sqrt{C}}{R_{x,s}}$ should be $M_s{}^3\sqrt{\frac{C}{R_{x,s}}}$.

NASA-Langley, 1965

Issued 4-26-65

NATIONAL AERONAUTICS AND SPACE ADMINISTRATION

TECHNICAL REPORT R-182

REYNOLDS NUMBER EFFECTS ON THE INDUCED PRESSURES OF CYLINDRICAL BODIES WITH DIFFERENT NOSE SHAPES AND NOSE DRAG COEFFICIENTS IN HELIUM AT A MACH NUMBER OF 24

By Richard D. Wagner, Jr., and Ralph Watson

ABSTRACT

Exact inviscid pressure distributions and shock shapes, obtained by the method of characteristics, are compared with experimental data. The results indicate a strong dependence of induced pressures upon Reynolds number, especially in the region immediately downstream of the nose-cylinder junction. The measured shock shapes revealed no discernible effect of Reynolds number variations.

NATIONAL AERONAUTICS AND SPACE ADMINISTRATION

TECHNICAL REPORT R-182

REYNOLDS NUMBER EFFECTS ON THE INDUCED PRESSURES OF CYLINDRICAL BODIES WITH DIFFERENT NOSE SHAPES AND NOSE DRAG COEFFICIENTS IN HELIUM AT A MACH NUMBER OF 24*

By Richard D. Wagner, Jr., and Ralph Watson

SUMMARY

An experimental investigation has been conducted to determine the effects of Reynolds number variations on the induced pressures over flow-alined cylindrical models at a Mach number of 24. Theoretical nose drag coefficients between 0.2 and 1.2 were covered by the six pairs of models tested, one model of a pair having a conical nose and the other a contoured nose of the same drag. (Thus, in addition to investigating the blast-wave effect of nose drag on induced pressure over a fairly wide range of nose drag coefficients, the secondary effect of nose shape on induced pressures at a constant nose drag was also obtained.)

Induced pressures immediately downstream of the nose-cylinder junction were found to be greatly affected by Reynolds number variations, and the extent to which this effect was felt downstream was found to depend upon the nose drag of a given model. A simple flow model is proposed to account for these Reynolds number effects by analogy with the problem of hypersonic flat-plate boundary-layer-displacement effects. Comparison with the data shows that the effects can be estimated with reasonable accuracy by this simple approach.

Experimental shock shapes are compared with exact inviscid solutions. The results indicate no discernible effects of Reynolds number on the shock shape.

---

*The information in this report is largely based on a thesis entitled "An Experimental Investigation of Nose Shape and Reynolds Number Effects on Induced Pressures at a Mach Number of 24" submitted by Richard D. Wagner, Jr., in partial fulfillment of the requirements for the degree of Master of Science in Aeronautical Engineering, Virginia Polytechnic Institute, Blacksburg, Virginia, August 1962.

INTRODUCTION

Much effort has been expended in the study of induced pressures on blunt-nose bodies. (See refs. 1 to 6, for example.) The blast-wave theory, as applied to aerodynamics in reference 1, has provided an extremely useful tool for the prediction of pressures in the induced-pressure region. This theory, though inadequate for direct calculations, affords good correlating parameters for induced pressures on blunt cylinders and plates. In particular, the results of reference 2 indicate that the blast-wave parameter yields a good correlation of induced pressures beyond 1 body diameter downstream of the nose-cylinder junction; nearer the nose-cylinder junction the correlation fails, and, other than by involved numerical calculation, no simple technique exists for estimating induced pressures in this region.

The present investigation is an outgrowth of the study presented in reference 3 wherein the effects of nose drag and nose shape on the induced pressures on various 1/8-inch-diameter cylinders were studied at Mach numbers of 17 and 21. The results of reference 3 revealed a need for further study of the factors governing the pressure distribution in the region immediately downstream of the nose-cylinder junction, and their relationship, if any, to the concepts afforded by the blast-wave theory. (Blast-wave theory implies that induced pressures are independent of nose shape.) The present study was conducted in the Langley 22-inch helium tunnel on scale models of the configurations used in reference 3; however, the models were 24 times larger in diameter to allow detailed pressure measurements to be made in the region of interest. Tests were conducted at various Reynolds numbers at a Mach number of 24. Pressure distributions were obtained on the nose as well as in the induced-pressure region to about 4 to 5 body diameters downstream of the nose-cylinder junction, with particular emphasis being given to the initial induced-pressure region.

SYMBOLS

$C = \dfrac{\mu_w T_s}{\mu_s T_w}$

$C_{D,n}$ nose drag coefficient

C_p pressure coefficient

d maximum model diameter

f nose fineness ratio

G defined by equation (5)

K_4 coefficient in equations (8) and (10) ($K_4 \approx 1.0$ for helium; $1.2 \gtrsim K_4 \gtrsim 1.0$ for air)

M	Mach number
M_{av}	average cross-section Mach number
n	exponent in power-law fit to pressure distribution
p	pressure
p_b	pressure due to blunt leading edges
r	nose radius (fig. 4)
$R_{d,\infty}$	free-stream Reynolds number based on maximum body diameter
R_x	Reynolds number based on x-dimension
T	temperature
x,y	Cartesian coordinates (fig. 4)
x_s	surface distance from nose-cylinder junction along cylindrical afterbody
y_b	distance along y-axis from body center line to surface
y_{sh}	shock displacement measured from axis of symmetry
γ	ratio of specific heats
δ	surface inclination with respect to free stream
δ^*	boundary-layer displacement thickness
μ	viscosity
$\overline{\chi}$	Lees-Probstein interaction parameter, $\frac{M^3\sqrt{C}}{R_x}$

Subscripts:

max	maximum
s	evaluated for inviscid flow on downstream side of nose-cylinder junction
t	stagnation
tc	corrected for transverse curvature

w wall of body

∞ free-stream value

TEST APPARATUS

Tunnel

This investigation was conducted in the Langley 22-inch helium tunnel, a closed-cycle facility described in reference 7. A schematic diagram of the tunnel is shown in figure 1. Helium is supplied from a high-pressure tank farm

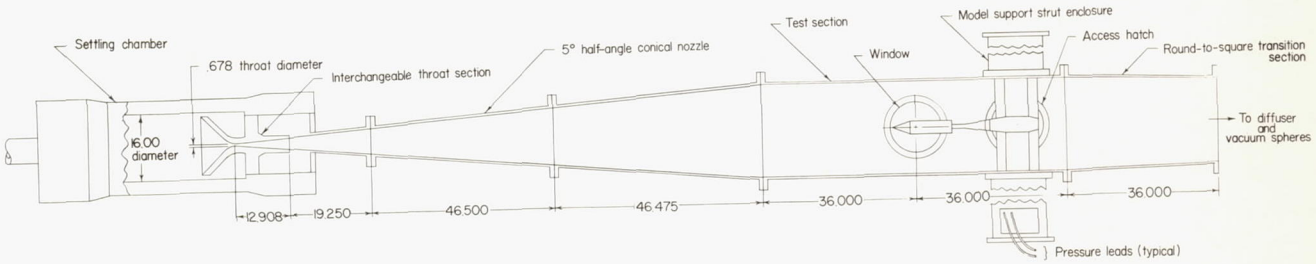

Figure 1.- Schematic diagram of the Langley 22-inch helium tunnel. (All dimensions are in inches.)

at about 5,000 psig; the stagnation pressure is regulated by an automatic control valve and the operating pressures are normally in the range from 500 to 3,000 psig. The helium in the stagnation chamber expands through a 5° half-angle conical nozzle into a constant 22-inch-diameter test section. Downstream of the test section is a variable-area diffuser from which the helium exhausts into two 60-foot-diameter vacuum spheres. Recompression and purification of the helium, followed by return to the tank farm, complete the closed cycle.

Tunnel Calibration

In order to conduct tests at different Reynolds numbers but at a fixed free-stream Mach number, the Langley 22-inch helium tunnel was calibrated to determine the Mach number distribution at various stations in the test section and at four stagnation pressures. A survey rake consisting of seven pitot tubes alined in a plane and spaced at 2-inch intervals was used in the calibration. The Mach number distributions in horizontal planes, on the test-section center line and 4 inches above and below the center line, were determined at stagnation pressures of 500, 1,000, 2,000, and 3,000 psig for various tunnel stations. The pitot pressures were measured with diaphragm-type gages that gave an estimated accuracy in the Mach number value of ± 0.2. The correction factors of reference 8 were used to correct for real-gas effects due to the high stagnation pressures.

The cross-section Mach number distributions at three tunnel stations and at stagnation pressures of 500 and 2,000 psig are shown in figure 2. Above each

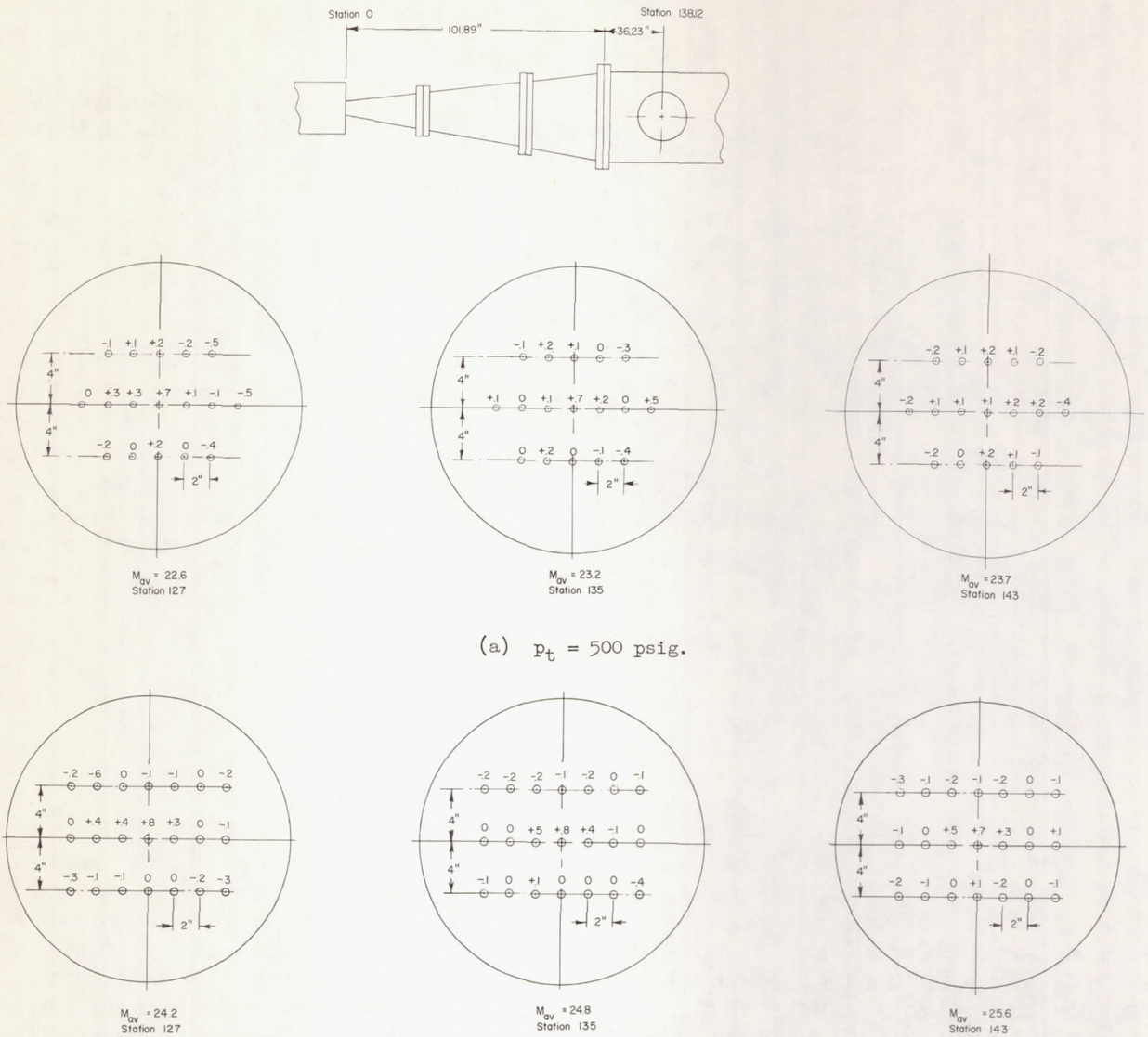

(a) p_t = 500 psig.

(b) p_t = 2,000 psig.

Figure 2.- Tunnel calibration. T_t = 50° F. (Value above each pitot-tube location denotes deviation from average cross-section Mach number.)

pitot-tube location is given the deviation of the measured Mach number from the average cross-section Mach number. The Mach number distributions obtained at stagnation pressures of 1,000 and 3,000 psig are similar to those at 500 and 2,000 psig and, for this reason, are not shown. The results presented in figure 2 indicate that the test-section core (the region not influenced by the boundary layer on the tunnel wall) is about 10 to 12 inches in diameter, and, in most cases, the Mach number near the center line is slightly higher than throughout the remainder of the usable core.

Since, in the present tests, the models were located on the center line of the tunnel and since the models had relatively small fineness ratio and diameter, the center-line Mach number would appear more representative for analysis of the data than the average cross-section Mach number. In figure 3 the test-section center-line Mach number is plotted at various stations and stagnation pressures. The Mach number gradient in the test section is, at most, about 0.12 per inch for the different stagnation pressures. Although conical-flow effects (test-section Mach number gradient and flow divergence) are known to affect induced pressures, it can be concluded from reference 5 that the effect is insignificant for axisymmetric configurations having a fineness ratio of the present test models. Therefore, it was not considered necessary to correct the measured pressures for conical-flow effects.

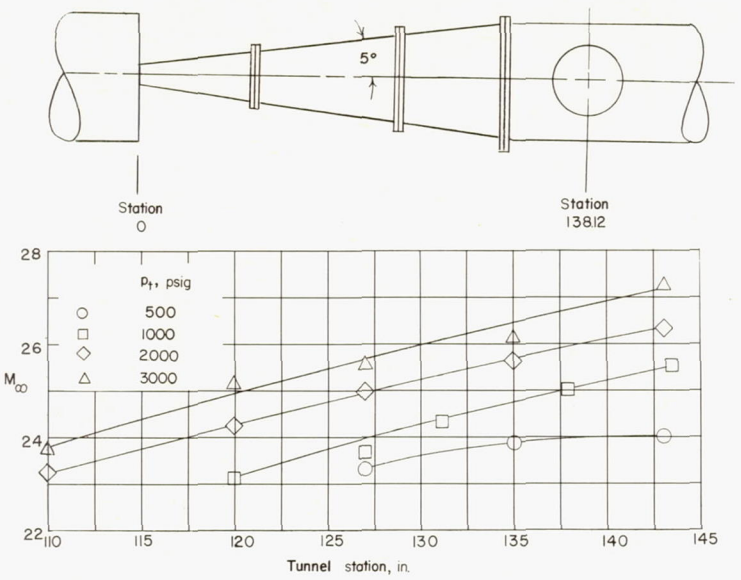

Figure 3.- Center-line Mach number distribution at various stagnation pressures.

Models

The models studied in this investigation are shown in figure 4. The 12 nose shapes consisted of six pairs, both models of a pair having the same theoretical nose drag but different shape. Six of the noses had a contoured shape; the remaining six were conical, each cone having a drag coefficient the same as a corresponding contoured nose shape. The theoretical nose drag was obtained by cone theory for the cone shapes (ref. 9) and by generalized Newtonian theory for the contoured shapes (ref. 10). The theoretical nose drag coefficients of the six pairs were 1.2, 1.0, 0.8, 0.6, 0.4, and 0.2.

Three of the six contoured nose shapes were spherical segments, one of which had a conical skirt with a 15° semivertex angle; the remaining three were parabolic. (See fig. 4.) The equation of the generating curve for the three contoured pointed shapes is

$$\frac{y}{d} = \frac{1}{f}\frac{x}{d}\left(1 - \frac{1}{2f}\frac{x}{d}\right) \qquad (1)$$

where x and y are Cartesian coordinates, f is the nose fineness ratio, and d is the maximum diameter. At the nose-cylinder junction, the pointed noses were tangent to the cylindrical afterbody. The nose fineness ratios were chosen as $f = 0.89$, 1.17, and 1.77 so as to obtain the desired drag coefficients. See reference 3 for details.

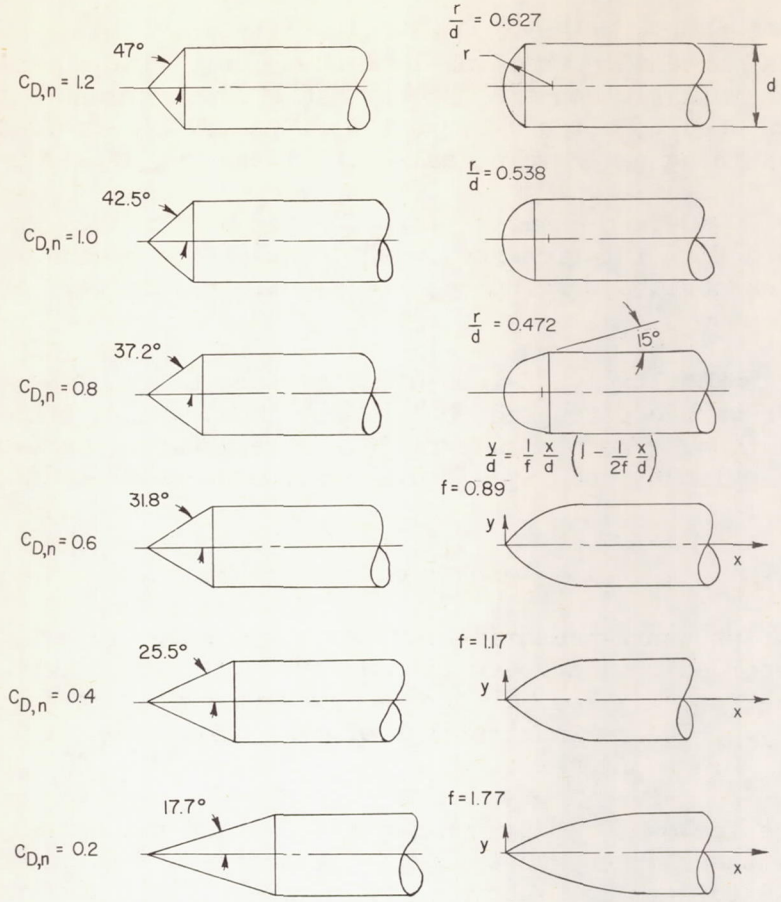

Figure 4.- Nose shapes of models studied.

The sketch of figure 5 illustrates the model construction. Twelve models were 3 inches in diameter with an overall length of 17 inches. The conical

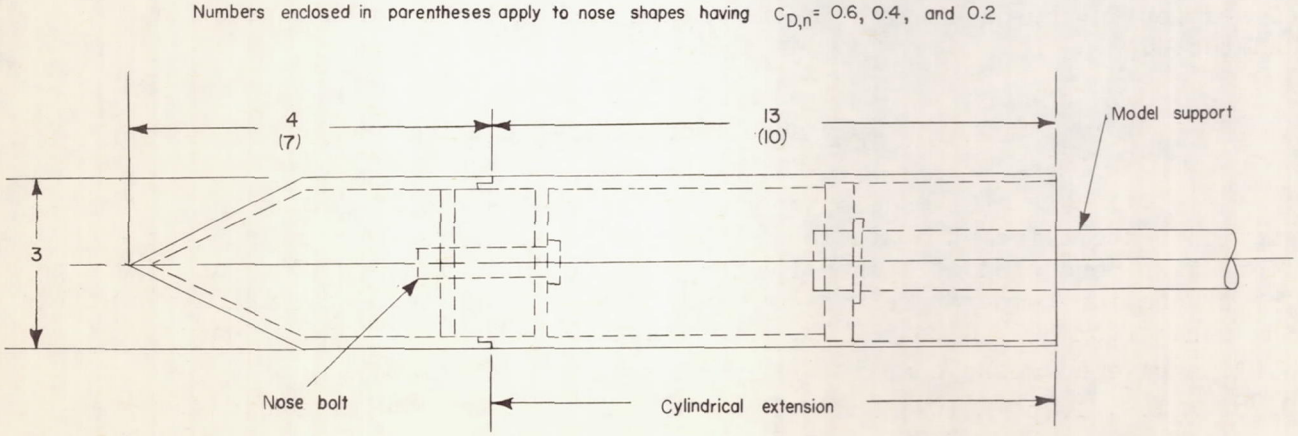

Figure 5.- Typical model construction. (All dimensions are in inches.)

and contoured nose shapes with the higher drags ($C_{D,n}$ = 1.2, 1.0, and 0.8) had a common cylindrical extension that was 13 inches long. The nose shapes with the lower drags were similarly constructed but had a 10-inch-long extension. An internal bolt was used to attach the nose portion of the models to the cylindrical extension. The joining parts were sealed and pressure checked prior to testing.

Orifices of 0.060-inch diameter were located alternately in meridian planes 45° apart to avoid flow interference on the nose of the models. The orifices on the cylindrical extensions were not as closely spaced and were alined in one meridian plane.

In addition to the twelve 3-inch-diameter test models, two smaller models of 1/2-inch diameter were constructed to increase the Reynolds number range covered in this investigation. These smaller models were 1/6-scale models of the $C_{D,n}$ = 1.2 cone-cylinder and $C_{D,n}$ = 0.2 contoured-nose—cylinder models.

Instrumentation

Two types of pressure-measuring devices were used. Pressures greater than 30 mm Hg were recorded on diaphragm transducers having an accuracy of ±2 percent of the full-scale rating. Four different gages were used so as to obtain maximum possible accuracy. (The maximum ratings of these four gages were 1, 2, 5, and 7.5 psia.)

For pressures below 30 mm Hg, an ionization gage employing a radioactive source to ionize the sampled gas was used. The gage operates on two ranges, 0 to 30 mm Hg and 0 to 3 mm Hg. Above 1 mm Hg, the gage is accurate to ±2 percent of the reading; below 1 mm Hg, the gage is accurate to ±5 percent of the reading. Inasmuch as the gage is of an ionization type, it is sensitive to gas composition. For example, the gage is approximately five times more sensitive to air than to helium. For this reason, extreme care was taken to eliminate all possible sources of leaks and contamination such as outgassing. Prior to testing, the models were thoroughly cleaned and placed in a vacuum tank for outgassing. When installed in the tunnel, the model tubing was kept under vacuum between tests. Small amounts of scatter in the data may be attributed to small leaks which were otherwise undetected.

Test Conditions and Procedure

For all tests the models were alined at zero angle of attack on the test-section center line at a station corresponding to a free-stream Mach number of 24. Tests were conducted at stagnation pressures of 600, 1,000, 2,000, and 3,000 psig. The stagnation temperature was constant for any given test and was always within the range from 500° R to 520° R. For the 3-inch-diameter models, these test conditions give Reynolds numbers, based on maximum body diameter, of 0.529×10^6, 0.882×10^6, 1.764×10^6, and 2.646×10^6 for the tests with stagnation pressures of 600, 1,000, 2,000, and 3,000 psig, respectively. The 1/2-inch-diameter models were tested at a stagnation pressure of 600 psig, corresponding to a Reynolds number, based on maximum body diameter, of 0.0882×10^6.

Prior to testing, the tunnel was purged with helium, and solenoid valves connecting the ionization gages and model tubing to a vacuum pump were opened. These valves remained open for approximately 4 seconds after flow was established to insure that only helium was present in the model tubing and ionization gages. The outputs of the diaphragm transducers and the ionization gages were recorded on magnetic tape at 3-second intervals throughout the tests to assure that the pressures had settled out to a constant value. With the use of the tunnel diffuser, an operating time of approximately 1 minute was possible, which was sufficient time for the pressures to settle out. (Flow breakdown would occur after about 40 seconds without the diffuser.)

RESULTS AND DISCUSSION

Pressure Distributions

The pressure distributions obtained on the models are shown in figure 6. These distributions are presented as a ratio of local static pressure to free-stream static pressure plotted against the nondimensional distance from the nose tip along the model center line. For the 3-inch-diameter models with the highest nose drag coefficient, surface pressures were measured at four stagnation pressures; for the other 3-inch-diameter models, surface pressures were measured at two stagnation pressures. In addition, the results of tests on the 1/2-inch-diameter models of the bluntest cone shape and the slenderest contoured shape are shown. (See data plotted for $R_{d,\infty} = 0.0882 \times 10^6$.) Also indicated in figure 6 are various theoretical inviscid predictions.

When possible, characteristics calculations were performed on an IBM 704 electronic data processing machine to determine the inviscid pressure distributions. These calculations were done with the intention of establishing a datum from which to assess Reynolds number effects on the pressure distribution. Calculations were performed in all cases except for the models with contoured nose shapes consisting of spherical segments. The characteristics method outlined in reference 9 for axisymmetric rotational flow was used.

Comparisons of the measured pressure distributions at different Reynolds numbers and those calculated by the characteristics theory give an excellent picture as to the regions influenced by viscous effects and the magnitude of these effects. In most cases, the pressure distribution over the nose of the models is insensitive to Reynolds number variations, at least in the range covered in this investigation. The pressure distribution on the cylindrical afterbodies indicates a marked dependence upon Reynolds number.

In the following discussion the results of the pressure measurements over the nose shapes (for which Reynolds number effects appear of minor importance) will first be considered. Attention will then be turned to the results obtained on the cylindrical afterbodies, which are of primary interest in this investigation.

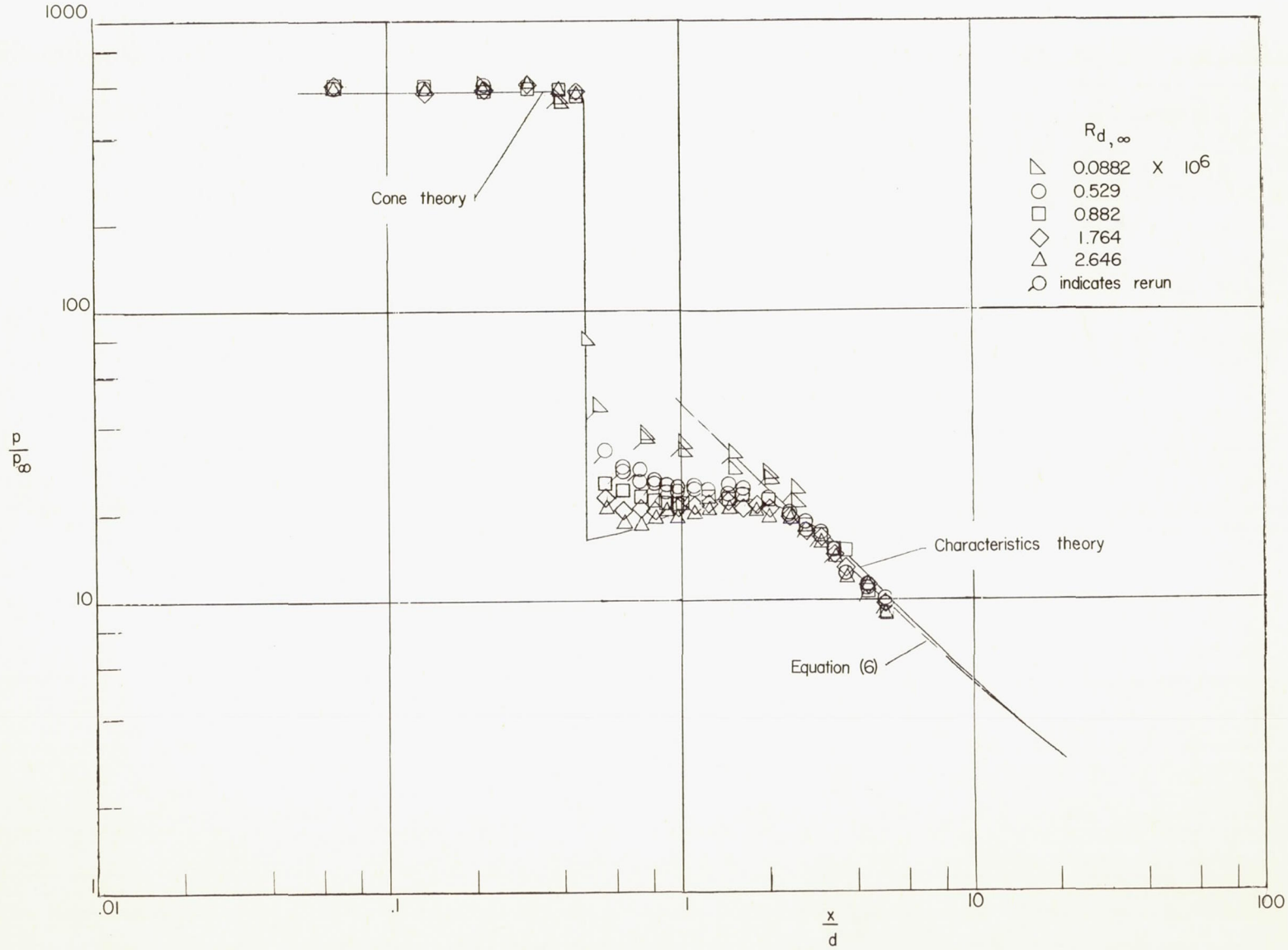

(a) Conical-nose model; $C_{D,n} = 1.2$.

Figure 6.- Pressure distribution over models. $M_\infty = 24$.

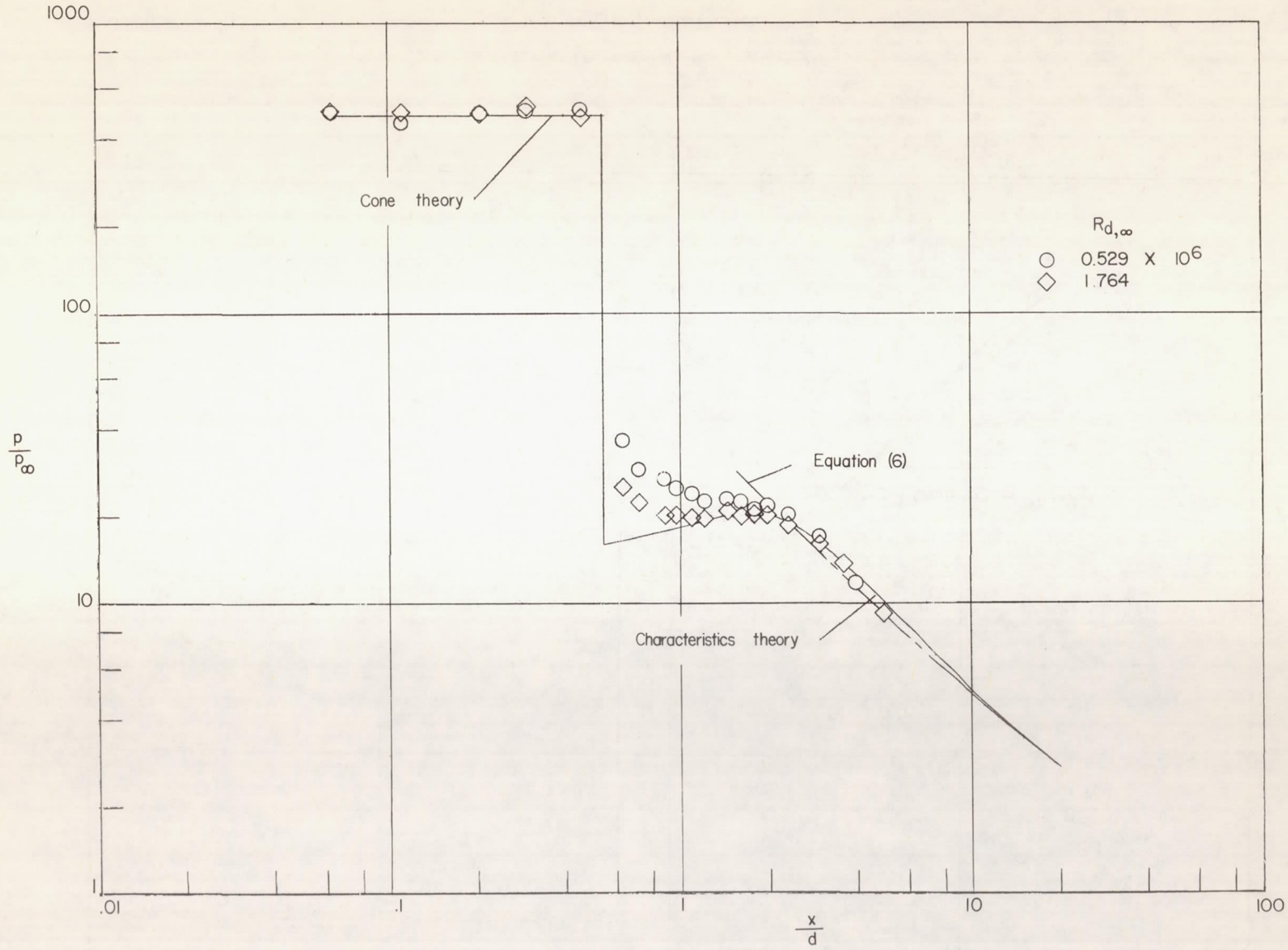

(b) Conical-nose model; $C_{D,n} = 1.0$.

Figure 6.- Continued.

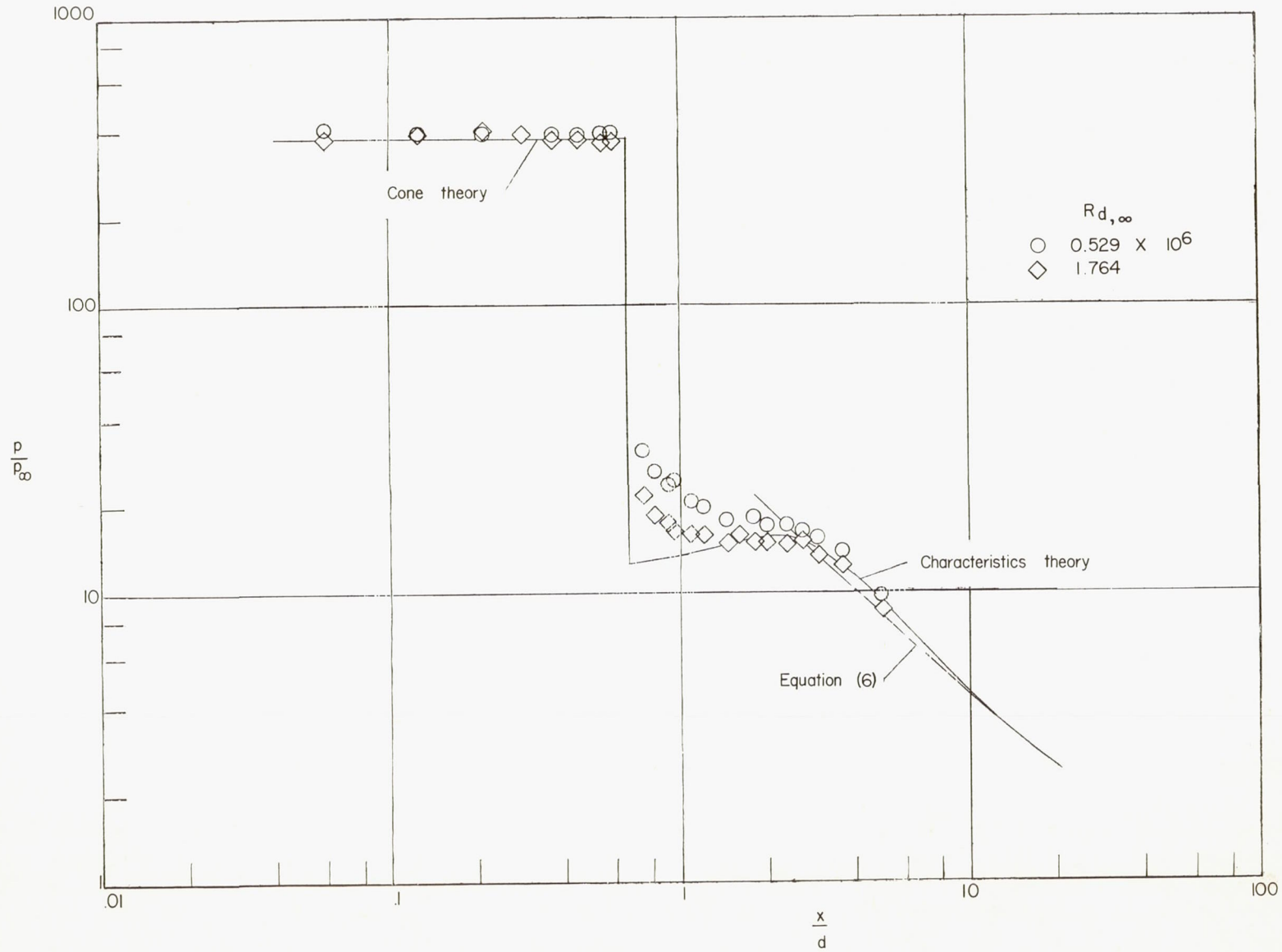

(c) Conical-nose model; $C_{D,n} = 0.8$.

Figure 6.- Continued.

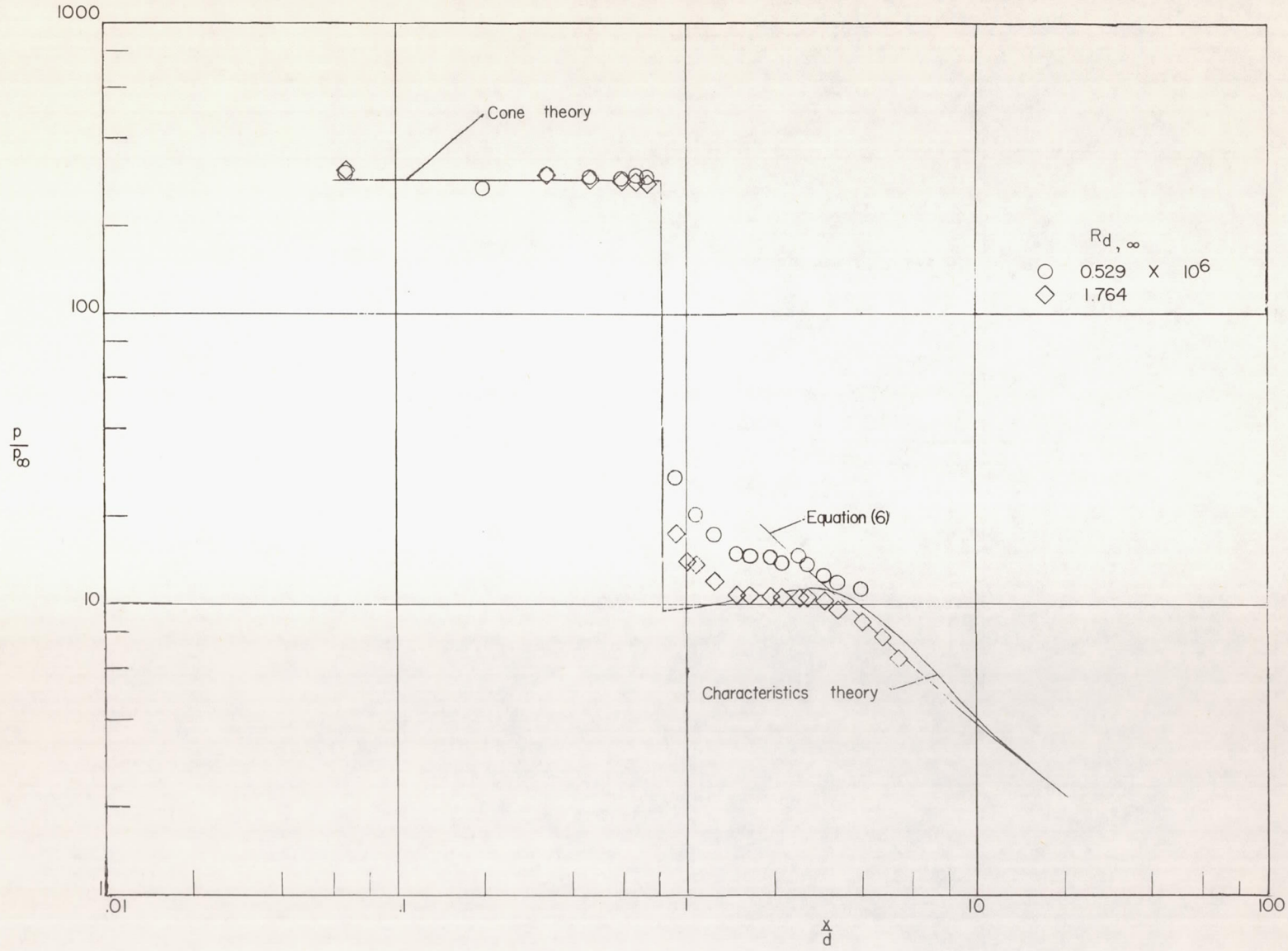

(d) Conical-nose model; $C_{D,n} = 0.6$.

Figure 6.- Continued.

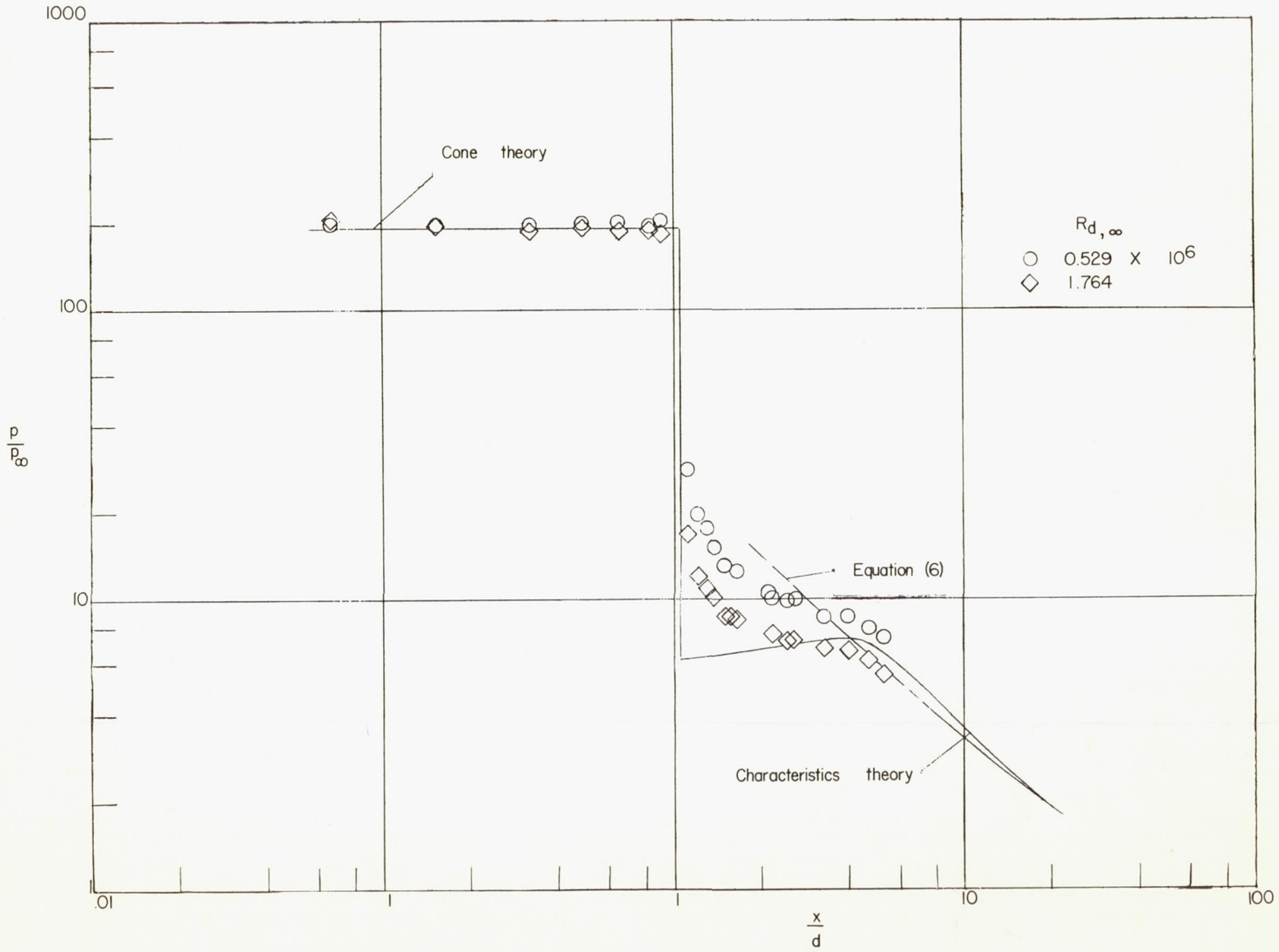

(e) Conical-nose model; $C_{D,n} = 0.4$.

Figure 6.- Continued.

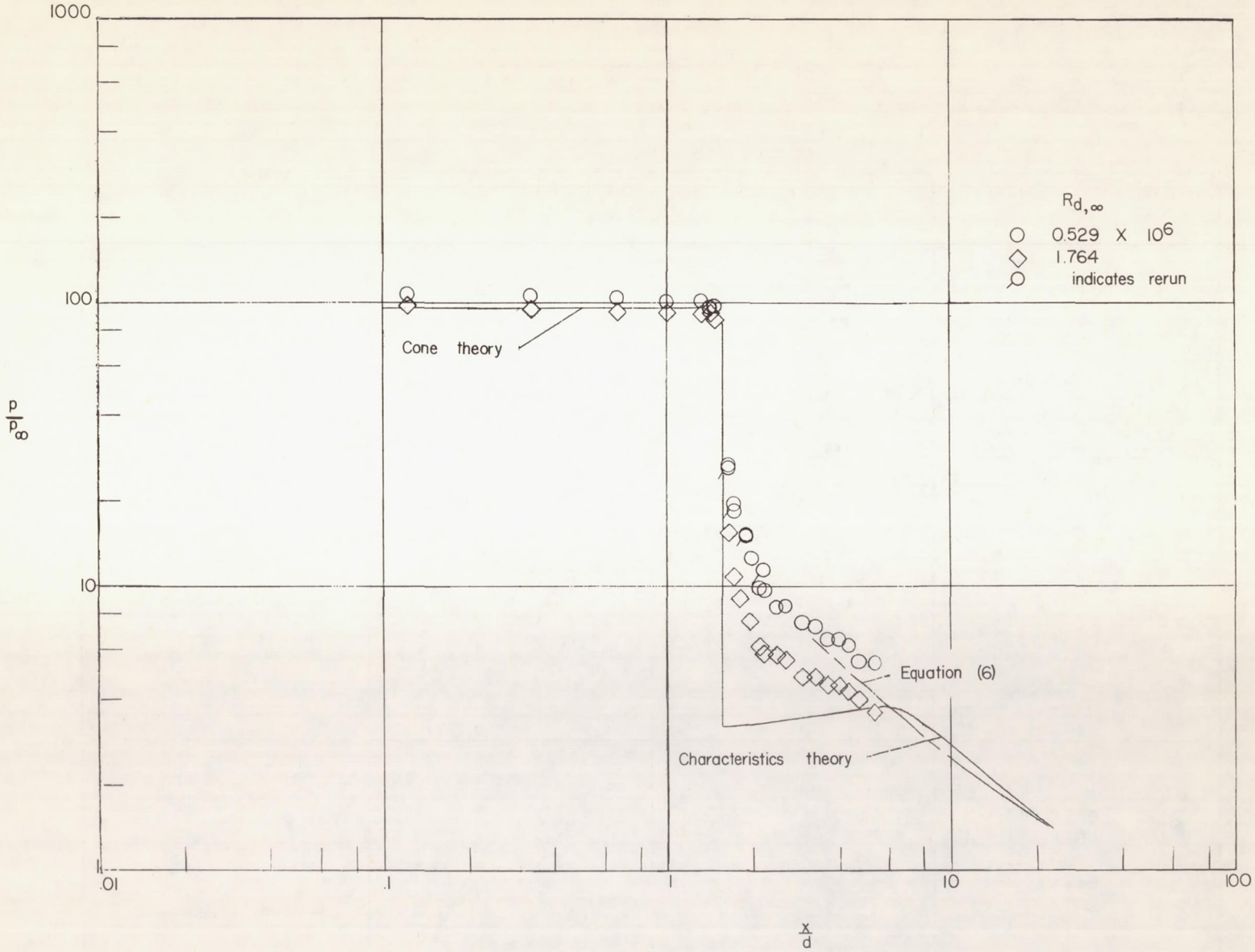

(f) Conical-nose model; $C_{D,n} = 0.2$.

Figure 6.- Continued.

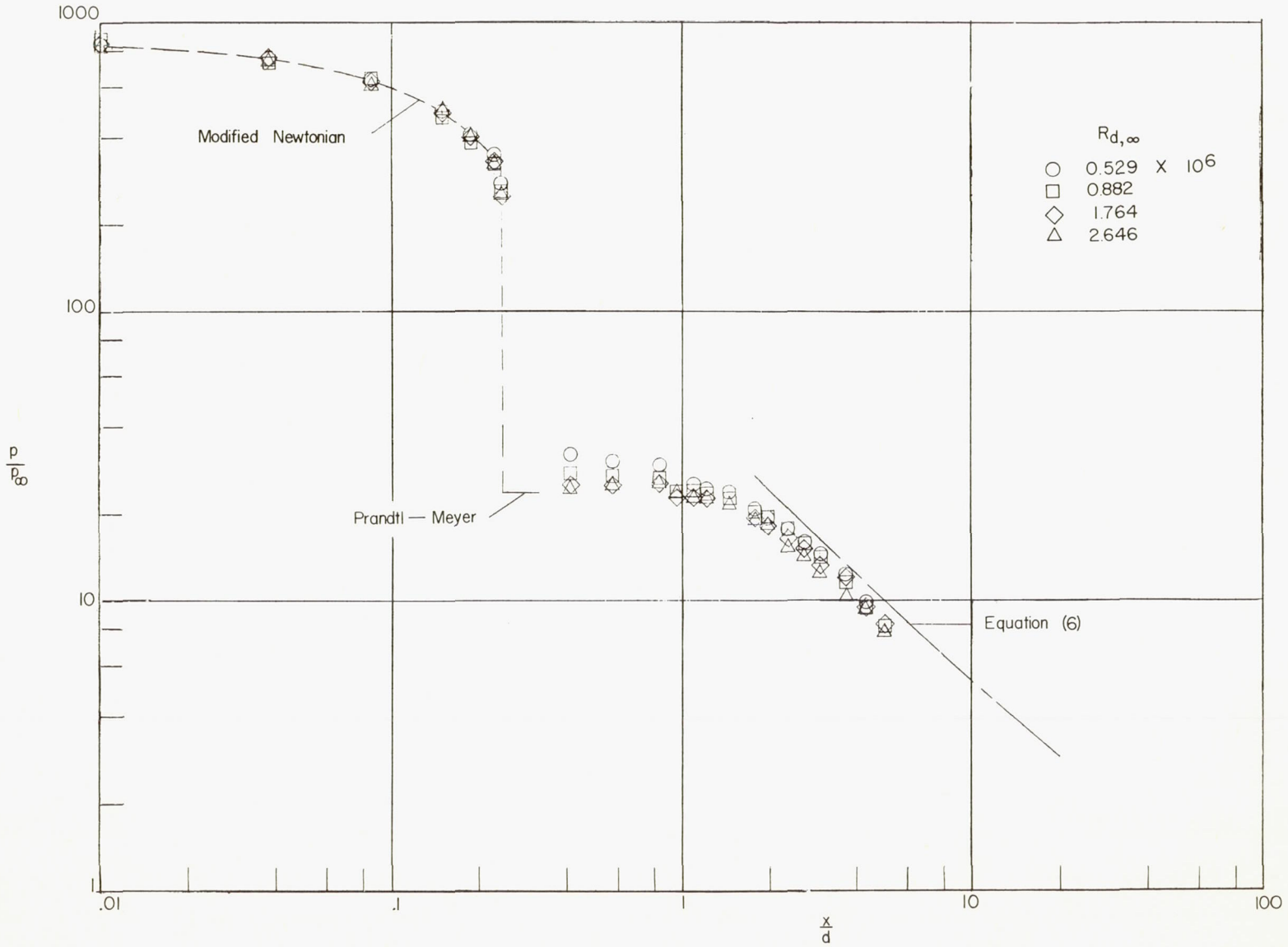

(g) Contoured-nose model; $C_{D,n} = 1.2$.

Figure 6.- Continued.

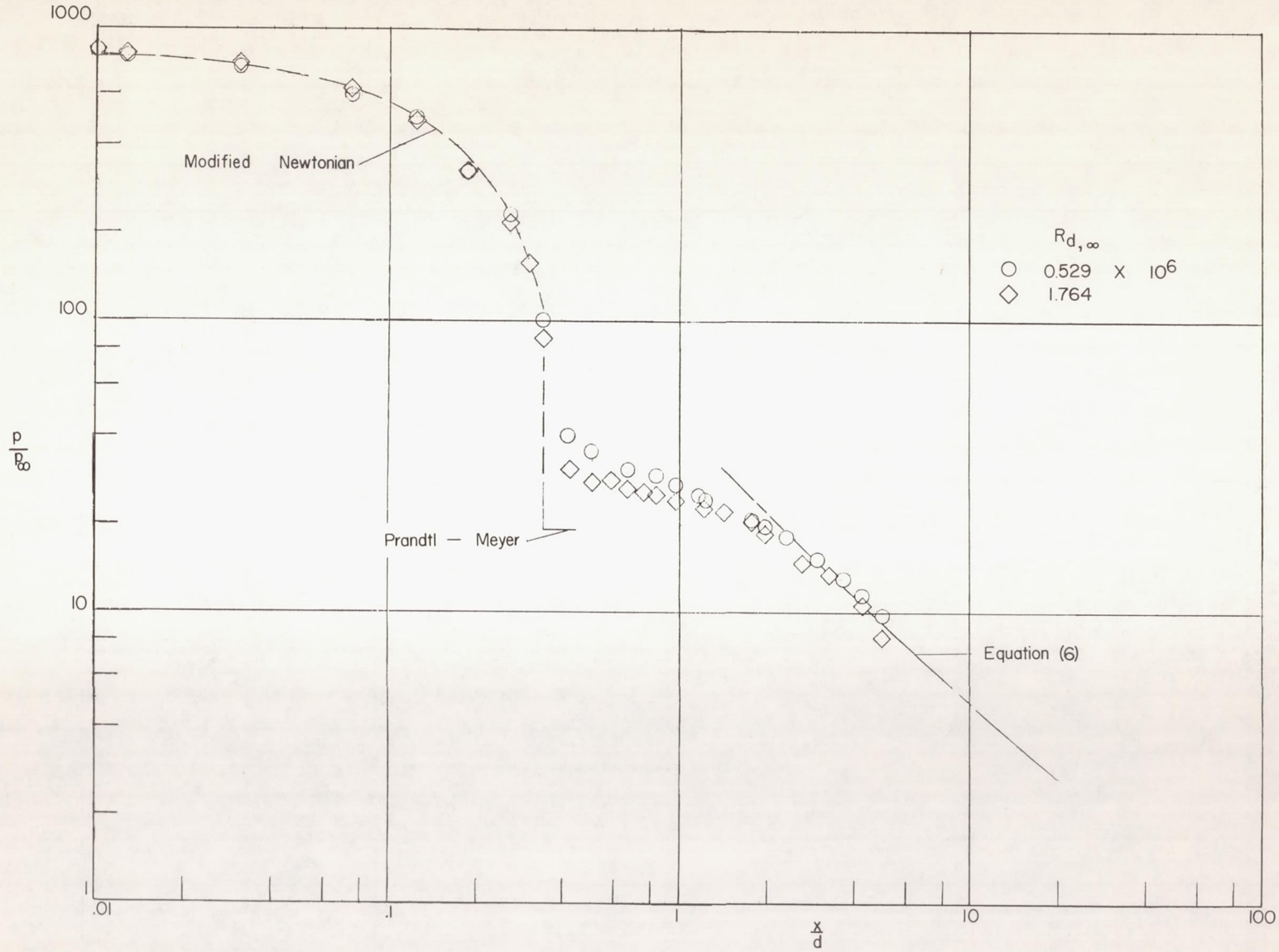

(h) Contoured-nose model; $C_{D,n} = 1.0$.

Figure 6.- Continued.

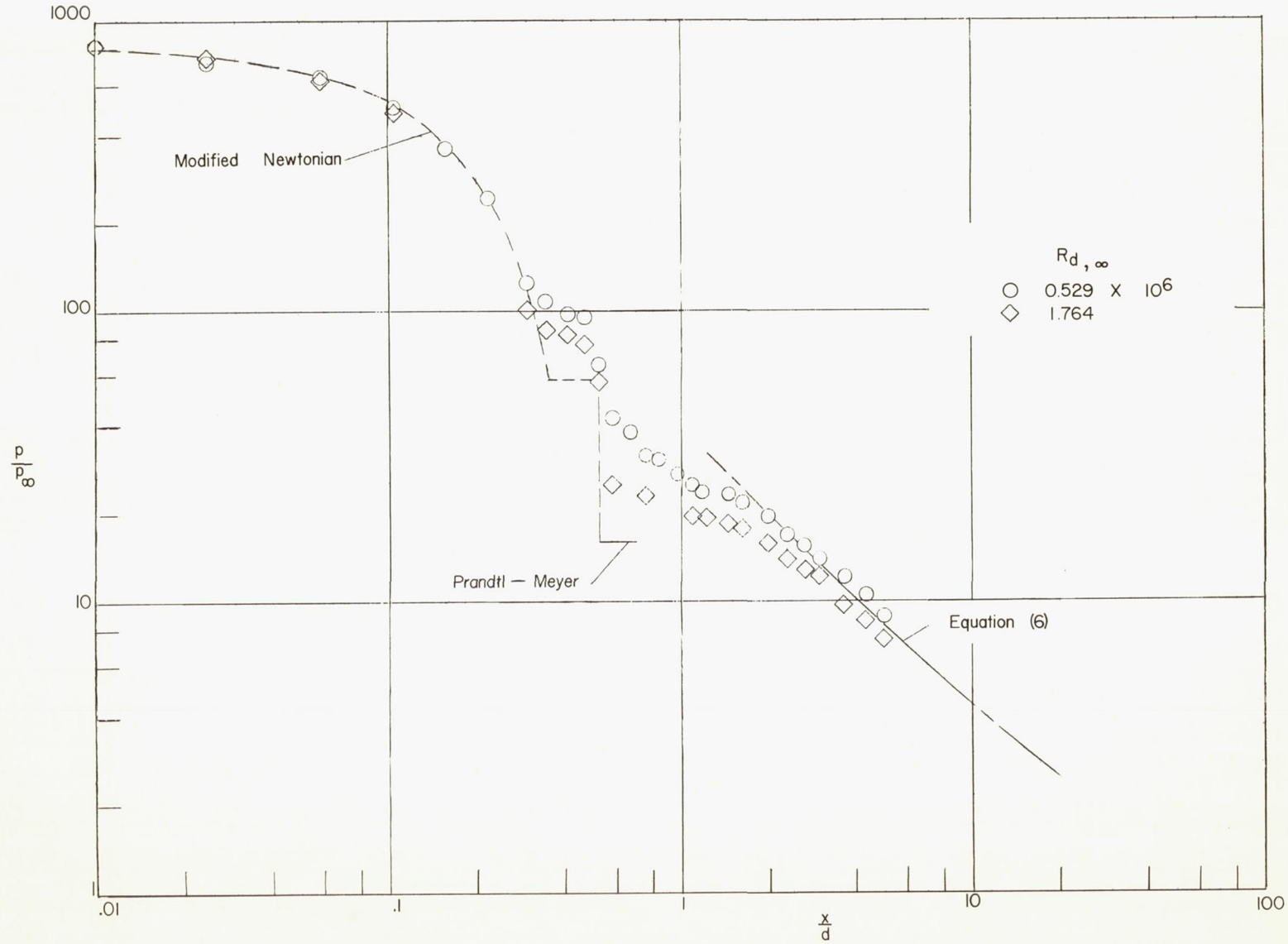

(i) Contoured-nose model; $C_{D,n} = 0.8$.

Figure 6.- Continued.

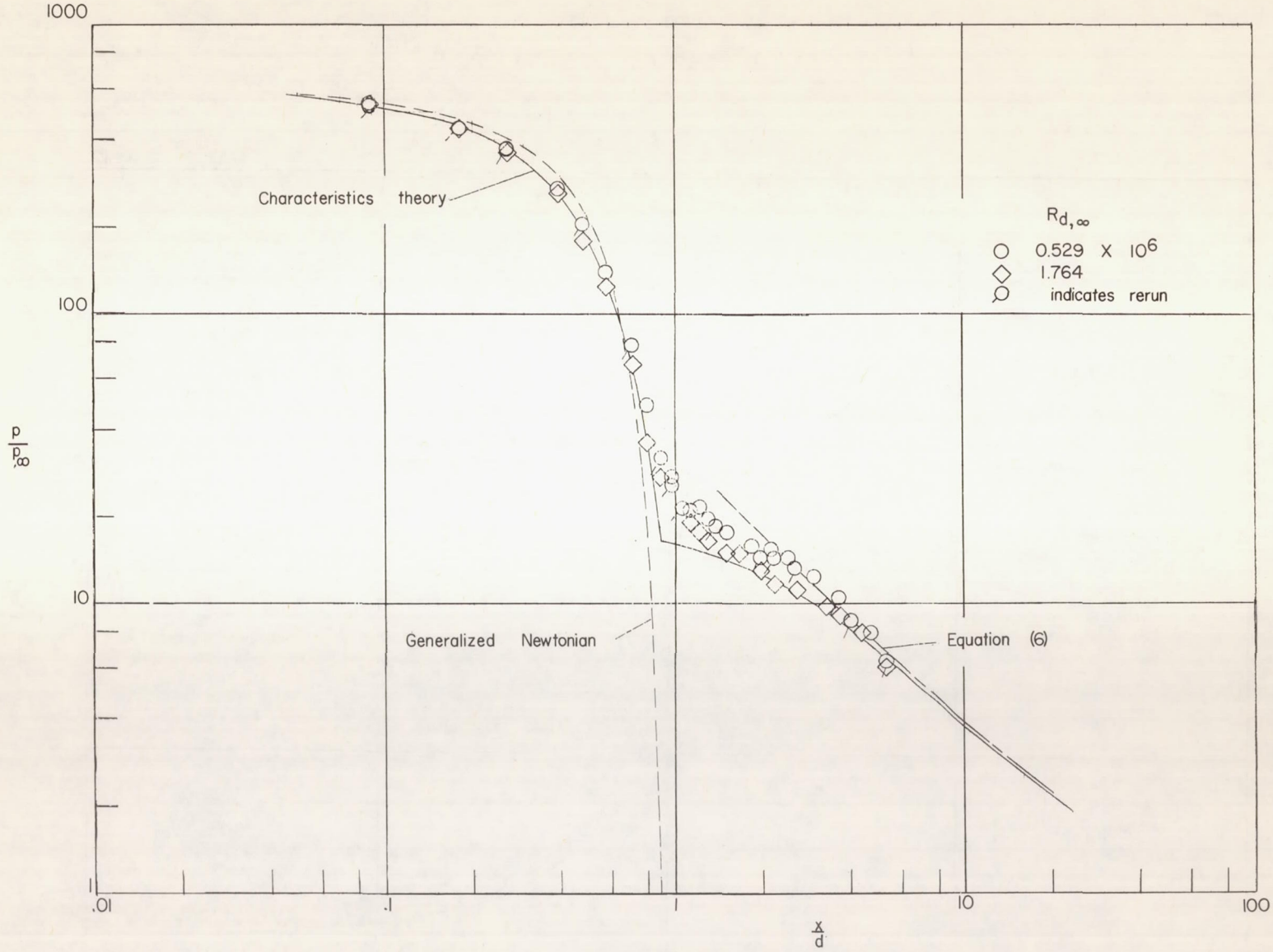

(j) Contoured-nose model; $C_{D,n} = 0.6$.

Figure 6.- Continued.

(k) Contoured-nose models; $C_{D,n} = 0.4$.

Figure 6.- Continued.

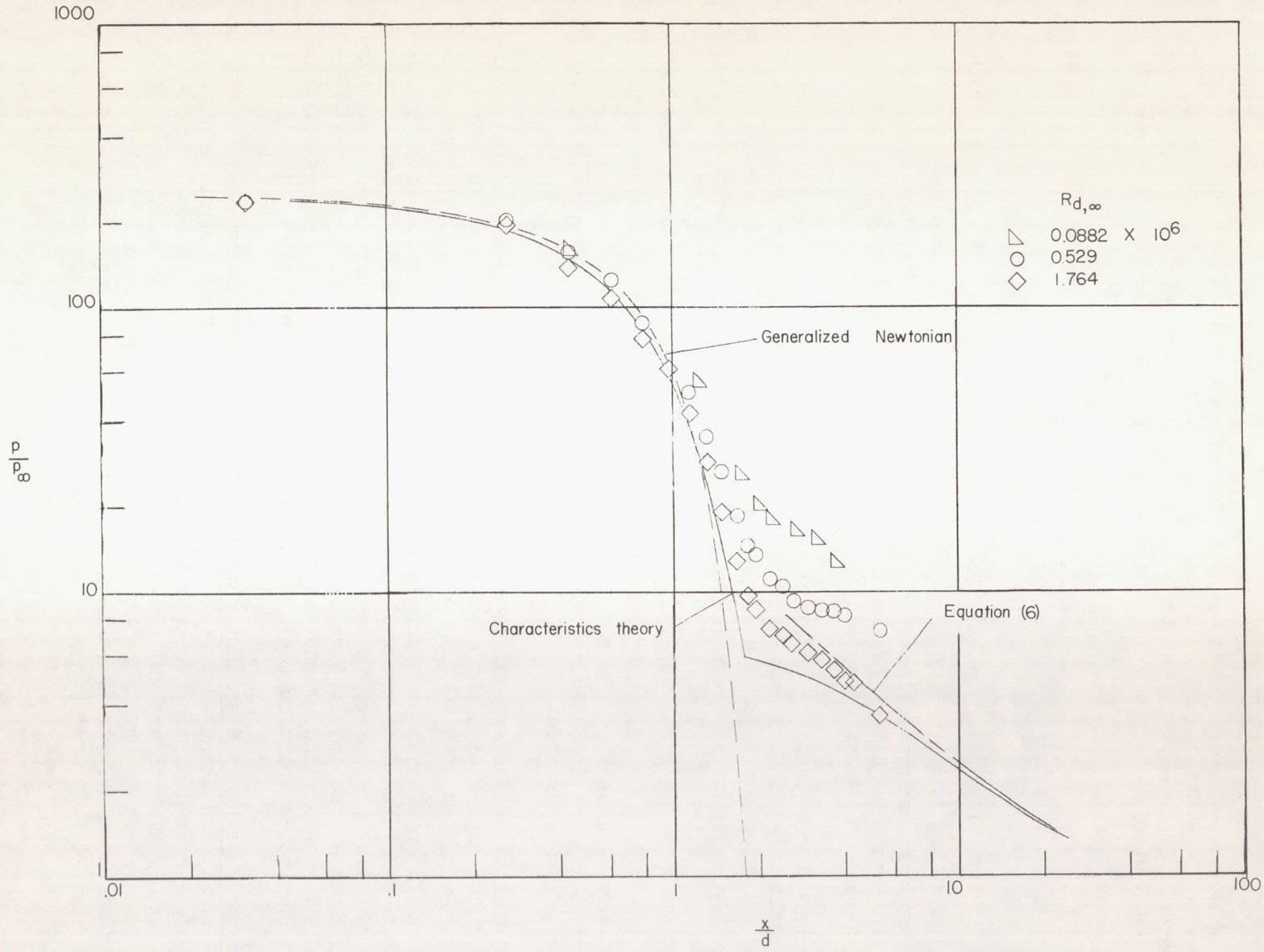

(l) Contoured-nose model; $C_{D,n} = 0.2$.

Figure 6.- Concluded.

Forebody pressure distribution.- As previously mentioned, the nose drag coefficients of the models, a parameter important in the blast-wave correlation of induced pressures, were taken as given by the generalized Newtonian theory of reference 10. For this reason, as well as for an indication of the usefulness of the theory, it is of interest to compare the present results with this theory. Generalized Newtonian theory gives the pressure distribution in the form

$$\frac{C_p}{C_{p,max}} = \frac{\sin^2\delta}{\sin^2\delta_{max}} \tag{2}$$

where δ_{max} is the maximum inclination of the body surface, δ is the local inclination of the body surface, and $C_{p,max}$ is taken as an exact value at the point of maximum surface inclination. For the conical and the blunt nose shapes, generalized Newtonian theory reverts to the well-established cone theory and modified Newtonian theory, respectively.

Figure 6 shows that the cone theory predicts the measured pressures on the conical noses. Reynolds number variations have no noticeable effect on the data except possibly on the cone with $C_{D,n} = 0.2$. For the contoured nose shapes, the theoretical distributions determined by the modified Newtonian theory show excellent agreement with the measured pressure distributions on the spherical parts of the contours with $C_{D,n} = 1.2$, 1.0, and 0.8. On the conical skirt of the nose with $C_{D,n} = 0.8$, some pressure variation with Reynolds number is observed; this variation may be caused by a more rapid boundary-layer growth induced by the sudden change in the inviscid pressure gradient from a strong favorable gradient to a zero pressure gradient.

The utility of the generalized Newtonian theory is well illustrated by comparison of the theory with the data and the characteristics solutions obtained on the contoured shapes with $C_{D,n} = 0.6$, 0.4, and 0.2. Except in the immediate vicinity of the nose-cylinder junction, little pressure variation with Reynolds number occurs and the data are well predicted by generalized Newtonian theory. At any rate, little accuracy is sacrificed in the use of generalized Newtonian theory in lieu of the involved characteristics solution, except perhaps in the region of the nose-cylinder junction where, in the absence of viscous effects, the characteristics solution would be necessary for an accurate prediction.

Afterbody pressure distribution.- In contrast to the observed effects on the nose pressures, the measured pressure distributions on the cylindrical afterbodies show a marked dependence upon Reynolds number. (See fig. 6.) These Reynolds number effects are quite similar for the models with equal nose drag; however, the extent to which the downstream region is influenced and the relative magnitude of these effects increase with decreasing nose drag. For the models with the highest nose drag $\left(C_{D,n} = 1.2\right)$, the high initial pressures on the afterbodies tend to suppress the viscous effects so that these effects subside beyond about 1 body diameter downstream of the nose-cylinder junction. As the nose drag decreases, these viscous effects are seen to be propagated farther downstream, and the magnitude of these effects relative to the inviscid pressure level appears

to increase. This is most pronounced on the conical-nose models. For the nose shapes with $C_{D,n} = 0.4$ and 0.2, Reynolds number variations are seen to affect the entire afterbody pressure distribution (in the region investigated) by a considerable amount.

A salient feature in the comparison of the data and characteristics theory is the observed recompression, at higher Reynolds numbers, downstream of the nose-cylinder junction on the models with conical noses with $C_{D,n} = 1.2$ and 1.0. (See figs. 6(a) and 6(b).) The data for the models with lower drag conical noses do not show the recompressions, which are smaller and apparently suppressed by the Reynolds number effects. (See figs. 6(e) and 6(f).)

Since characteristics solutions were not available for the contoured-nose models with $C_{D,n} = 1.2$, 1.0, and 0.8, the initial pressure on the cylindrical afterbody was calculated by a Prandtl-Meyer expansion at the nose-cylinder junction. In the Prandtl-Meyer expansion, the modified Newtonian pressure on the upstream side of the corner was used with the assumption of constant stagnation pressure equal to that behind the normal part of the bow shock. On the model with the highest nose drag (fig. 6(g)), where Reynolds number effects are not large, the Prandtl-Meyer expansion value for the initial pressure on the afterbody agrees well with the data. The pressures on the models with $C_{D,n} = 1.0$ and 0.8 differ considerably from the Prandtl-Meyer value.

Nature of Reynolds Number Effects and Prediction

Boundary-layer separation may be suspected as the cause for the viscous effects observed in the region immediately downstream of the nose-cylinder junction; however, oil-flow studies on the cone-cylinder with $C_{D,n} = 1.2$ and on a flat-face cylinder revealed no signs of separation. It would then appear that boundary-layer displacement would be the origin of these effects. In view of the complex nature of the flow field in this region, as characterized by the recompressions occurring on the cone-cylinder, an exact analysis of the viscous interaction in this region would appear quite unmanageable. Instead, good estimates of the boundary-layer induced pressures can be obtained with the use of a simple flow model and existing solutions for viscous interactions.

In reference 11, Bertram and Blackstock arrive at the following expressions describing the pressure increment due to a modified form of a weak boundary-layer interaction and that due to a strong interaction on a flat plate:

For the weak interaction,

$$\frac{p - p_s}{p_s} = \frac{\frac{\gamma G}{2}\bar{X}_s}{\sqrt{1 + \frac{\gamma G}{2}\bar{X}_s}}\left[1 + \frac{\frac{\gamma G}{2}\bar{X}_s}{2\left(1 + \frac{\gamma G}{2}\bar{X}_s\right)}\right] + \frac{\gamma + 1}{4\gamma}\frac{\left(\frac{\gamma G}{2}\bar{X}_s\right)^2}{1 + \frac{\gamma G}{2}\bar{X}_s}\left[1 + \frac{\frac{\gamma G}{2}\bar{X}_s}{2\left(1 + \frac{\gamma G}{2}\bar{X}_s\right)}\right]^2 \quad (3)$$

and, for the strong interaction,

$$\frac{p - p_s}{p_s} = \frac{3}{4} G \bar{X}_s \sqrt{\frac{\gamma(\gamma + 1)}{2}} \tag{4}$$

where G is given by (for a Prandtl number of 1.0)

$$G = 1.7208 \frac{\gamma - 1}{2} \left(\frac{T_w}{T_t} + 0.3895 \right) \tag{5}$$

The subscript s refers to the undisturbed stream, and $\bar{X}_s$ is the Lees-Probstein interaction parameter $\frac{M_s^3 \sqrt{C}}{R_{x,s}}$. In order to apply equations (3) and (4) to the present problem, the inviscid flow immediately downstream of the nose is approximated by a uniform stream of constant pressure equal to the inviscid pressure on the downstream side of the nose-cylinder junction. The stagnation pressure behind the initial part of the bow shock is also assumed to exist over the entire region of interest. As a further simplification, the influence of the nose on the boundary-layer growth is ignored and the effective origin of the boundary layer is taken at the nose-cylinder junction. For a discussion of boundary-layer growth over contoured nose shapes, see the appendix of this report.

The pressure distributions on the cylindrical afterbodies are again shown in figure 7 as a plot of p/p_∞ against the nondimensionalized surface distance from the nose-cylinder junction. Also shown are the pressure distributions obtained by adding the pressure increments due to boundary-layer displacements given by

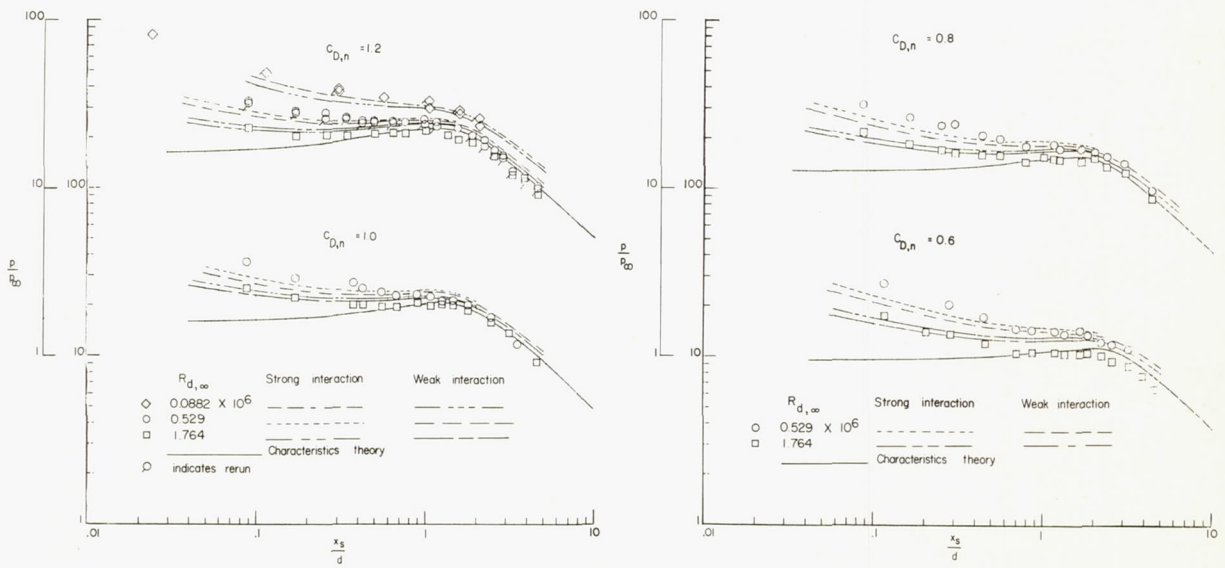

(a) Conical-nose models; $C_{D,n}$ = 1.2 and 1.0. (b) Conical-nose models; $C_{D,n}$ = 0.8 and 0.6.

Figure 7.- Pressures on cylindrical afterbodies.

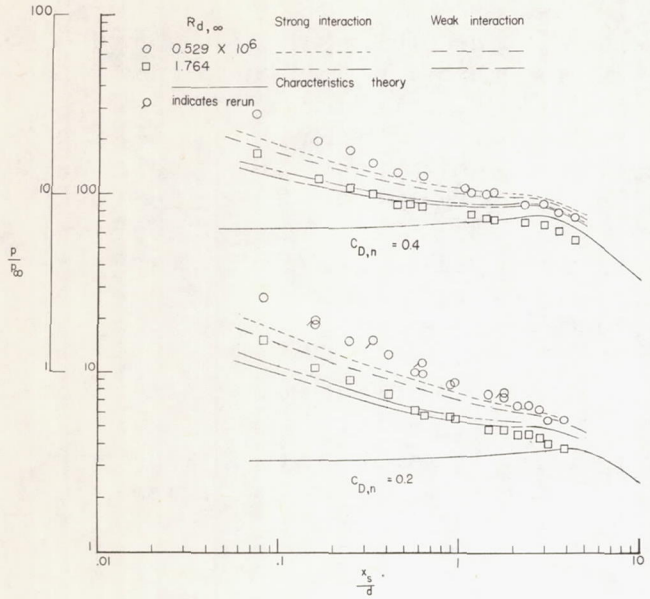

(c) Conical-nose models; $C_{D,n}$ = 0.4 and 0.2.

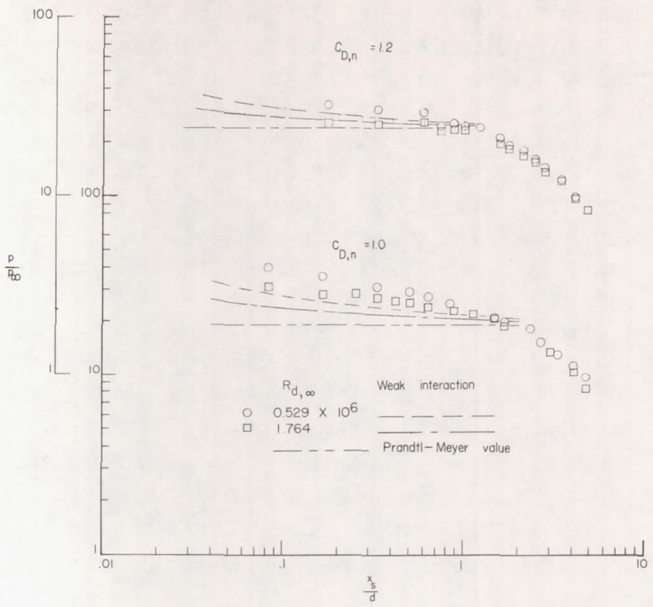

(d) Contoured-nose models; $C_{D,n}$ = 1.2 and 1.0.

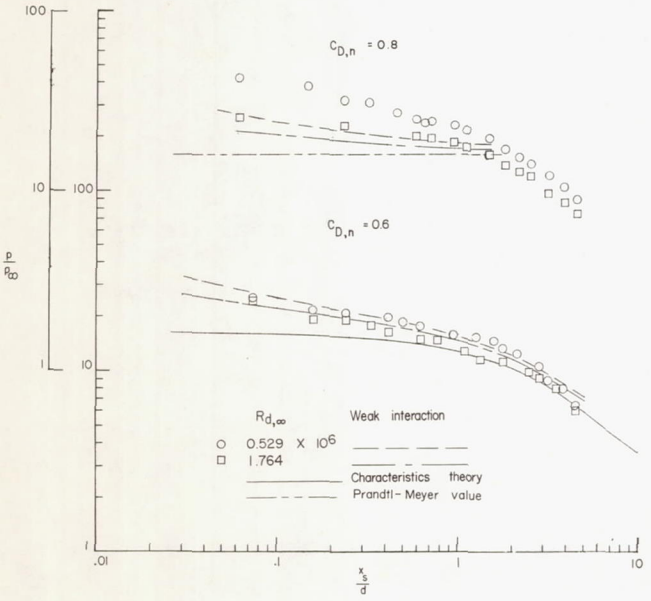

(e) Contoured-nose models; $C_{D,n}$ = 0.8 and 0.6.

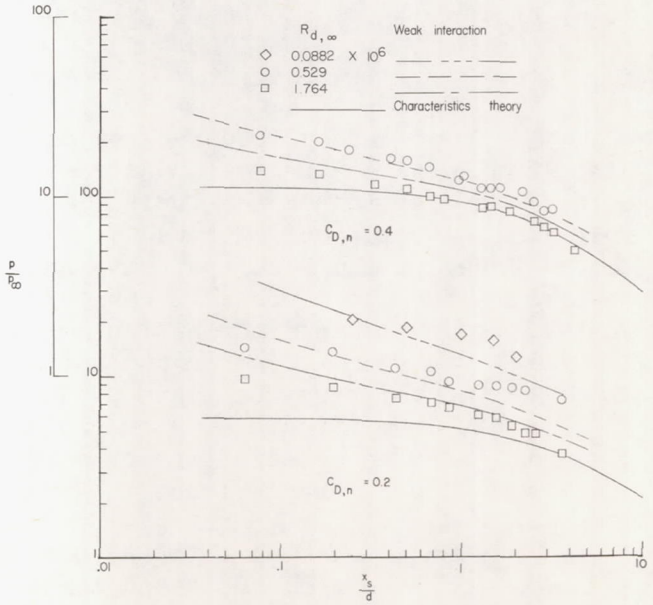

(f) Contoured-nose models; $C_{D,n}$ = 0.4 and 0.2.

Figure 7.- Concluded.

equations (3) and (4) to the characteristics solutions. In the cases of the models having spherical nose shapes, the curves were obtained by adding the pressure increments to the inviscid Prandtl-Meyer expansion value. Considering the simplicity of this approach, the agreement between the data and theory is relatively good. The strong interaction, in most cases, better represents the data on the models with conical noses, though only slightly different results are obtained for the weak interaction. For the models with conical noses, the agreement between theory and data is better for the higher nose drag coefficients than for the lower nose drag coefficients, probably because of the influence of the boundary layer on the nose of the model which would become larger for lower nose drag coefficients. For the models with contoured noses, the data are compared only with the weak-interaction solution since, as mentioned, only slightly different results were obtained with the strong-interaction solution.

The data for the spherical-nose models (figs. 7(d) and 7(e)) are underestimated by the theory, especially for the cases of $C_{D,n} = 1.0$ and 0.8. The agreement with data could probably be improved by using an exact initial pressure in the inviscid Prandtl-Meyer expansion and a rigorous theory for the inviscid pressure distribution. The viscous effects on the conical skirt for $C_{D,n} = 0.8$ would, however, complicate this problem.

The data for the slender contoured-nose models $\left(C_{D,n} = 0.6,\ 0.4,\ \text{and}\ 0.2\right)$ are well represented by the weak-interaction solution. At $R_{d,\infty} = 0.0882 \times 10^6$ and 0.529×10^6 for $C_{D,n} = 0.2$ (fig. 7(f)), the pressure distribution does not decay as rapidly as the interaction solution indicates, probably because of the effective origin assumed for the boundary layer. In this case, there were sizable viscous effects slightly upstream of the nose-cylinder junction.

The above method requires, of course, a knowledge of the inviscid pressure distribution in the region downstream of the nose-cylinder junction. At present, the prediction of the inviscid pressure distribution entails involved numerical calculations inasmuch as no simple theoretical approaches are available. However, the results of the analytical study of reference 6 offer a possible alternate approach. For cylinders with geometrically similar nose shapes, the pressure distribution, when referenced to the maximum surface pressure, was found to correlate not only over the nose portions but also well into the induced-pressure region. In addition, this form of correlation tends to eliminate the effects of Mach number and gas properties (see ref. 6), and seems to offer the possibility of cataloging the induced-pressure distribution in regard to nose shape alone.

In order to examine this approach, the characteristics solutions for the six cylinders with conical noses and three cylinders with contoured noses are shown in figure 8 in terms of the ratio of local to maximum surface pressure. For both nose geometries the correlation is very good, though superior for the cone-cylinder. The correlation achieved on the nose portions is implied in generalized Newtonian theory, but of greater interest herein is the correlation within the induced-pressure region. In reference 6, only two cone angles were considered, 53° and 46°; the present results show that the correlation exists over a wide range of cone angles and includes the sharp-parabolic-nose cylinder. (Of

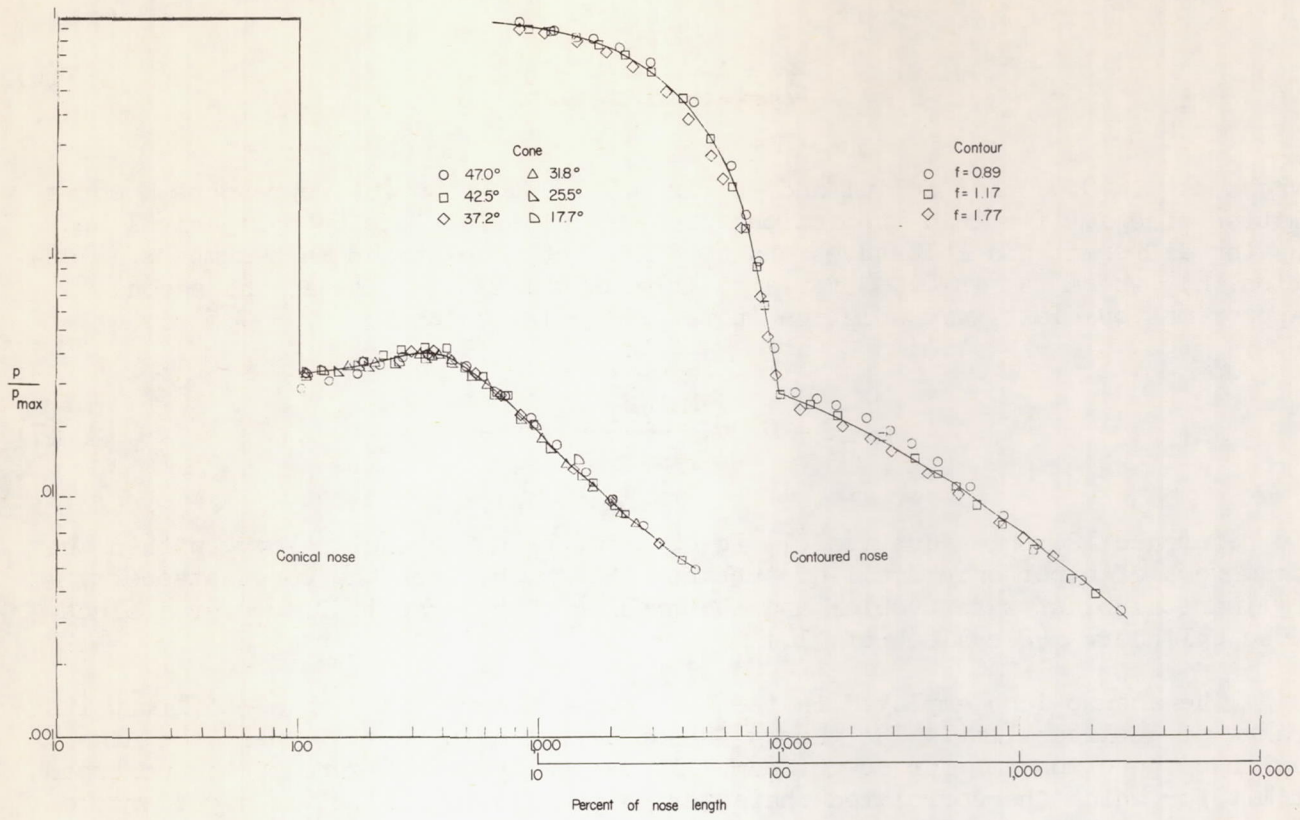

Figure 8.- Correlation of inviscid nose and afterbody pressures - conical and contoured nose shapes.

course there must exist a downstream limit to the correlation in the induced-pressure region because of the relatively common asymptotic pressure on the cylinders.)

Considered herein and in reference 6 have been only cylinders with attached bow shocks, and the extension to cases with detached shocks is not immediately apparent.

Reynolds Number Effects on the Blast-Wave Correlation

In the preceding discussion, the extent to which Reynolds number effects were observed downstream of the nose-cylinder junction was seen to depend, in part, upon the nose drag. Since, in some cases, these effects covered the entire region of induced pressures within the range of this investigation, the effectiveness of blast-wave theory for predicting induced pressures in regions where viscous effects are significant is questionable.

In figure 6 is shown the correlated characteristics equation derived by Van Hise (ref. 6), which is expressed in terms of the blast-wave parameter $\frac{M_\infty^2\sqrt{C_{D,n}}}{x/d}$ as

$$\frac{p}{p_\infty} = A\frac{M_\infty^2\sqrt{C_{D,n}}}{x/d} + B \tag{6}$$

where A is 0.075 for helium and B is 0.55. Equation (6) represents a correlation of exact inviscid theoretical pressure distributions on cylindrical bodies having different nose bluntness and at different free-stream Mach numbers. Equation (6), where A is 0.060 for air, is essentially the same as the second-approximation blast-wave solution in reference 12, which for $\gamma = 7/5$ is

$$\frac{p}{p_\infty} = 0.067\frac{M_\infty^2\sqrt{C_{D,n}}}{x/d} + 0.44 \tag{7}$$

In reference 12, this equation (7) is obtained by using the analogy, within the framework of hypersonic small-disturbance theory, between the constant-energy cylindrical blast-wave problem and the problem of hypersonic flow over a blunt-nose cylinder. (See also ref. 1.)

The assumptions employed in the blast-wave theory are such as to limit its range of applicability. The theory is not expected to be valid near the nose-cylinder junction nor far downstream. As can be seen in figure 6, the upstream limit for which the correlated characteristics equation (6) gives a good representation of both the data and the characteristics solutions depends upon the nose drag, shape, and Reynolds number.

Several authors have indicated that though the blast-wave theory has definite upstream limits, the blast-wave parameter affords a good correlation of experimental data throughout a wider region than would be expected, even for nose drag coefficients as low as 0.2. (See refs. 2 and 3.) For example, in reference 3 it is concluded that beyond 1 diameter from the nose-cylinder junction, nose shape has no effect on induced pressures as implied in the blast-wave theory. In figure 9 are shown the measured pressure distributions plotted in terms of the ratio p/p_∞ against the blast-wave parameter as used in reference 3. (Ref. 3 uses the axial distance measured from the shoulder rather than from the nose tip. Also shown is the correlated characteristics eq. (6) with x/d measured from the shoulder. Using x_s/d in eq. (6) is inconsistent with the method by which the equation is obtained, but would introduce only small differences where it would be expected to apply. See fig. 9.) In general, the effects of nose shapes are not significantly large beyond 1 diameter from the nose-cylinder junction, and for the high-nose-drag shapes $(C_{D,n} = 1.2$ and $1.0)$, the data would indicate a fair correlation with the blast-wave parameter. However, for the low-nose-drag shapes, the present data along with that of reference 3 clearly illustrate that a correlation of data with the blast-wave parameter, without due regard to Reynolds number effects, may be quite erroneous, as has been indicated previously in the paper. Reynolds numbers much lower than those of the present investigation may also affect the correlation of pressures on the high-nose-drag shapes.

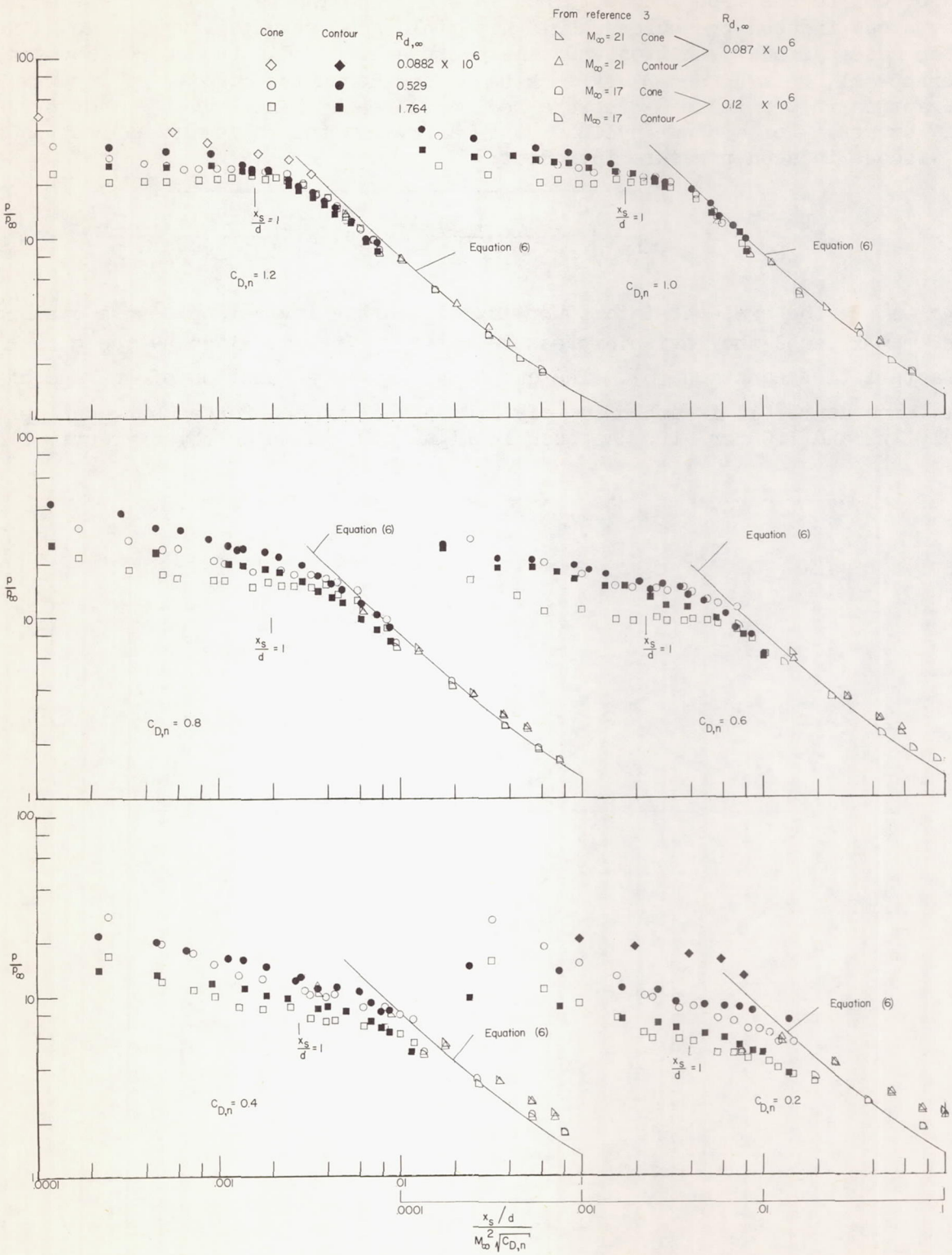

Figure 9.- Pressure distributions plotted against blast-wave parameter.

Of course the approach, outlined in the preceding section, for estimating the viscous induced pressures should not yield good results very far downstream of the nose-cylinder junction where large pressure gradients occur. However, in reference 11, Bertram and Blackstock have considered the effects of viscous interaction in the induced-pressure region where the blast-wave type of pressure decay occurs. For a blunt cylinder they arrive at the following expression for the viscous induced pressure increment:

$$\frac{p - p_\infty}{p_\infty} = \frac{1}{2}\left\{\sqrt{\left(\frac{p_b}{p_\infty}\right)^2 + \frac{\gamma(\gamma+1)}{2}\left[(1-n)K_4\right]^2\left(\frac{G^2 M_\infty^6}{R_{d,\infty}\, x/d}\right)} - \frac{p_b}{p_\infty}\right\} \tag{8}$$

where n is the exponent in a power-law fit to the inviscid pressure distribution $p \propto x^n$, and the inviscid pressure ratio p_b/p_∞ is given by the correlated characteristics equation (6). The quantity K_4 is a function of n and the wall temperature; it is approximately 1.0 for helium and ranges between approximately 1.2 and 1.0 for air. As seen in figure 10, equation (8) overestimates the

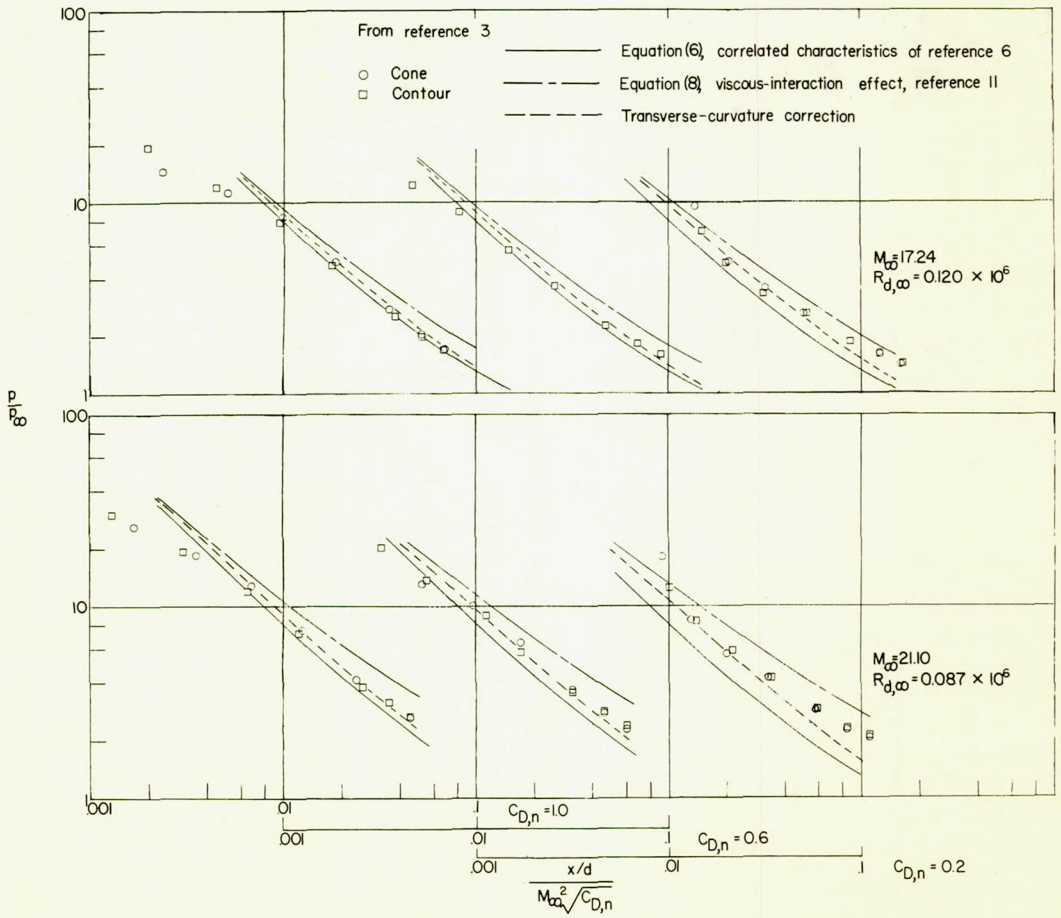

Figure 10.- Reynolds number effects in the blast-wave region of induced pressures for $C_{D,n}$ = 1.0, 0.6, and 0.2.

effects of viscous interactions when compared with the data of reference 3. An important effect which is not included in equation (8) is the effect of transverse curvature. An estimate of transverse curvature effects may be made with the use of the results of reference 13 in which was obtained the following expression for the boundary-layer displacement-thickness slope including the effect of transverse curvature:

$$\left(\frac{d\delta^*}{dx}\right)_{tc} = \frac{d\delta^*}{dx}\Bigg/\sqrt{1 + \frac{2\delta^*}{y_b}} \tag{9}$$

where δ^* is the boundary-layer displacement thickness. Although expression (9) is only an approximation and is not valid for large values of δ^*/y_b, it still should yield informative results. If δ^* in the correction factor of equation (9) is taken as that resulting for the viscous interaction without the effects of transverse curvature and if the relations of reference 11 are used (see eqs. (2) and (16) of this reference), the following approximation may be considered as a first-order correction to equation (8):

$$\left(\frac{p - p_\infty}{p_\infty}\right)_{tc} = \frac{\dfrac{p - p_\infty}{p_\infty}}{1 + 4GK_4 \dfrac{x}{d} \dfrac{\overline{\chi}_\infty}{M_\infty \sqrt{\dfrac{p_b + (p - p_\infty)}{p_\infty}}}} \tag{10}$$

This result is included in figure 10. As can be seen, the inclusion of the transverse curvature gives a more conservative estimate of the viscous induced pressures than that given by equation (8), and in most cases gives a good estimate of the measured viscous induced pressures.

Shock-Shape Studies

Typical schlieren photographs taken of each model at a stagnation pressure of 600 psig are shown in figure 11. Enlargements of these photographs were made and the shock shapes determined by measurement.

The blast-wave parameter for the correlation of shock shapes is $\frac{x}{d}\sqrt{C_{D,n}}$, not including the effects of Mach number which are small for free-stream Mach numbers above 20. (See ref. 6.) As for the pressure distributions, shock shapes should be independent of nose geometry in the region where blast-wave theory is expected to apply. Figure 12 represents a comparison of the experimental shock shapes with those obtained from the characteristics theory and from the correlated characteristics relation (see ref. 6):

$$\frac{y_{sh}}{d} = K\left(\frac{x}{d}\sqrt{C_{D,n}}\right)^{0.46} \tag{11}$$

The constant K is 0.98 for air and 1.07 for helium. The agreement of the shock shapes from characteristics solutions and the experimental data is excellent.

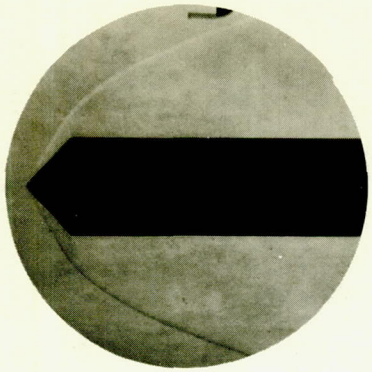

$C_{D,n} = 1.2$

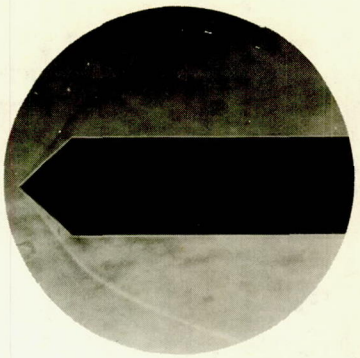

$C_{D,n} = 1.0$

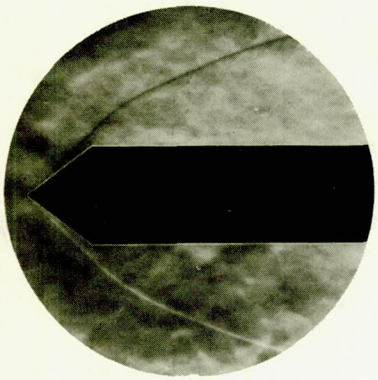

$C_{D,n} = 0.8$

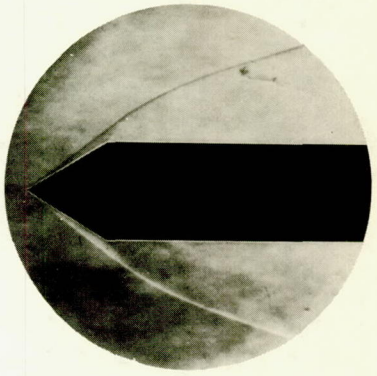

$C_{D,n} = 0.6$

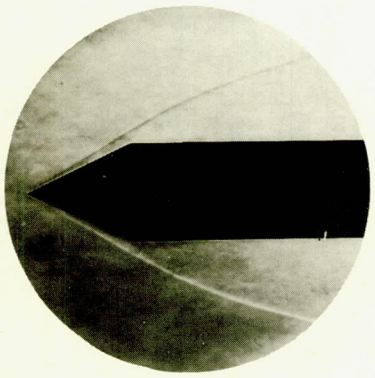

$C_{D,n} = 0.4$

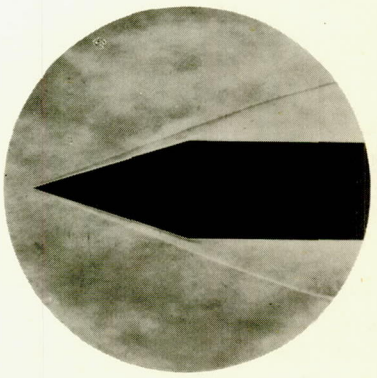

$C_{D,n} = 0.2$

(a) Conical-nose models. L-63-3182

Figure 11.- Schlieren photographs of models at $M_\infty = 24$ and $R_{d,\infty} = 0.529 \times 10^6$.

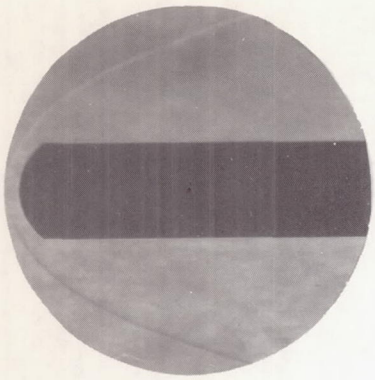

$C_{D,n}$ = 1.2

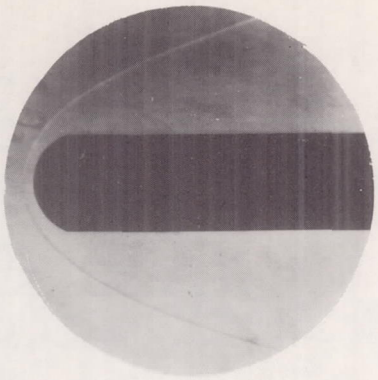

$C_{D,n}$ = 1.0

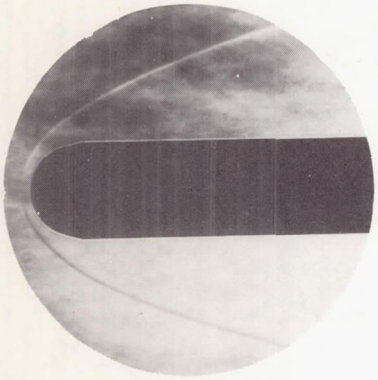

$C_{D,n}$ = 0.8

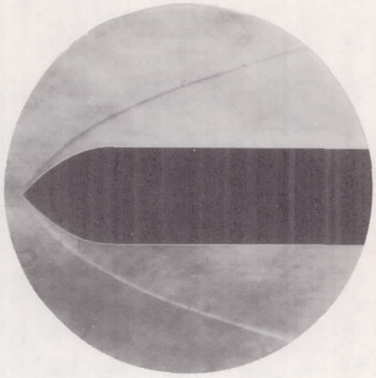

$C_{D,n}$ = 0.6

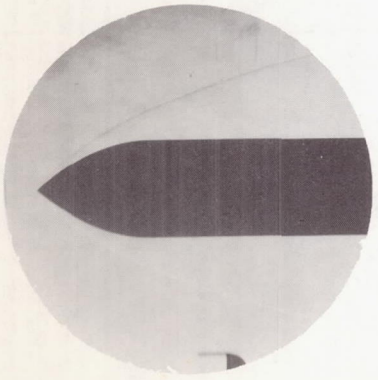

$C_{D,n}$ = 0.4

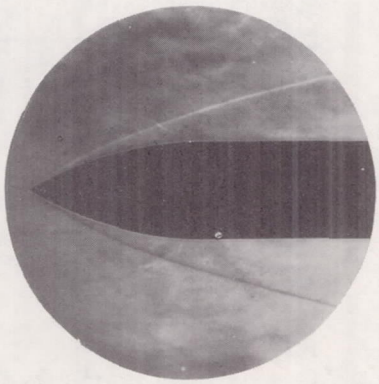

$C_{D,n}$ = 0.2

(b) Contoured-nose models. L-63-3183

Figure 11.- Concluded.

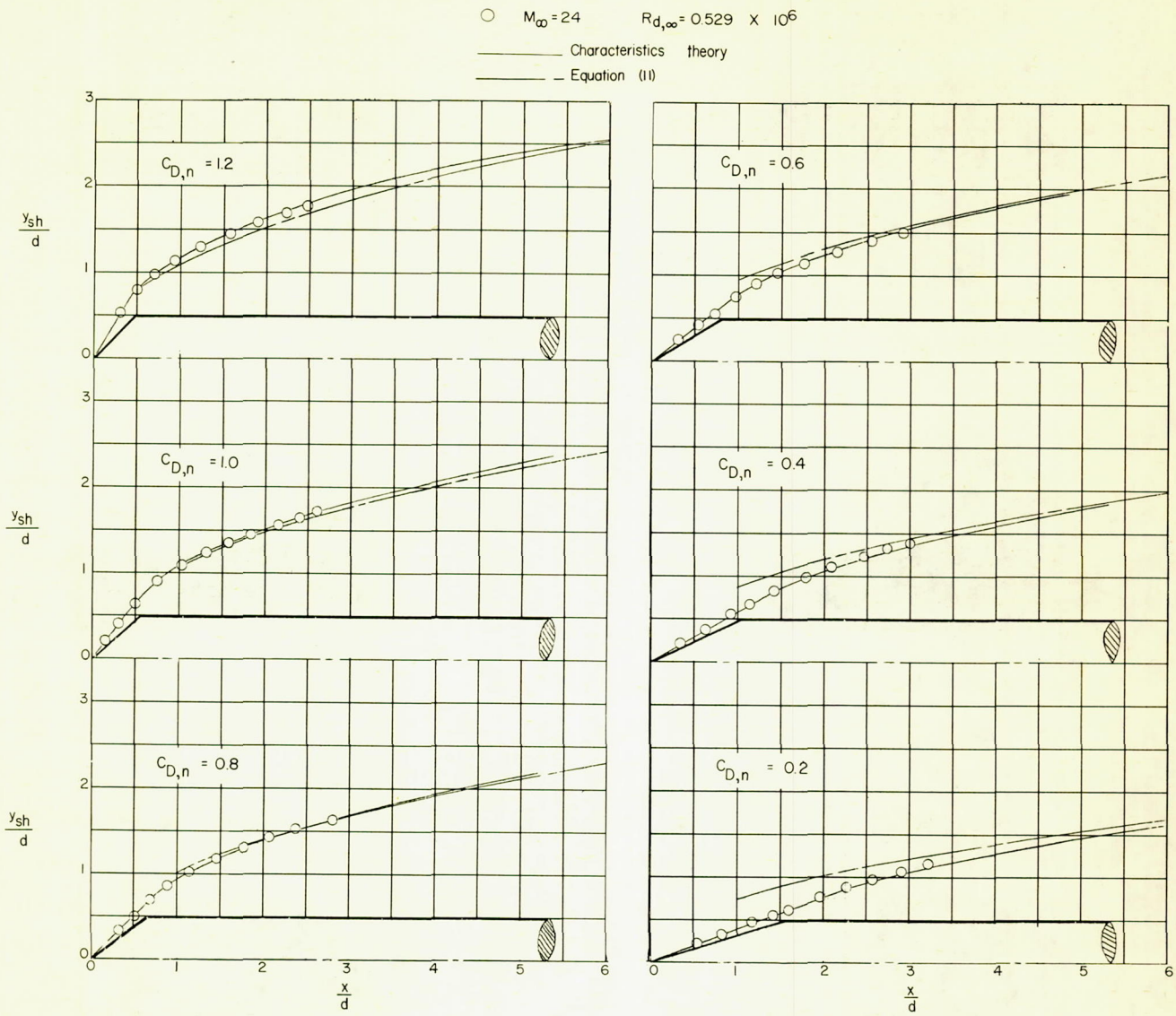

(a) Conical-nose models.

Figure 12.- Comparison of theoretical and experimental shock shapes.

Although the data are shown only at the Reynolds number of 0.529×10^6, Reynolds number variation would not be expected to noticeably affect the shock shape; this is evident in the comparison of the data and the rigorous inviscid theory. The results in figure 12 also give a good indication of the adequacy of the correlated characteristics equation (11).

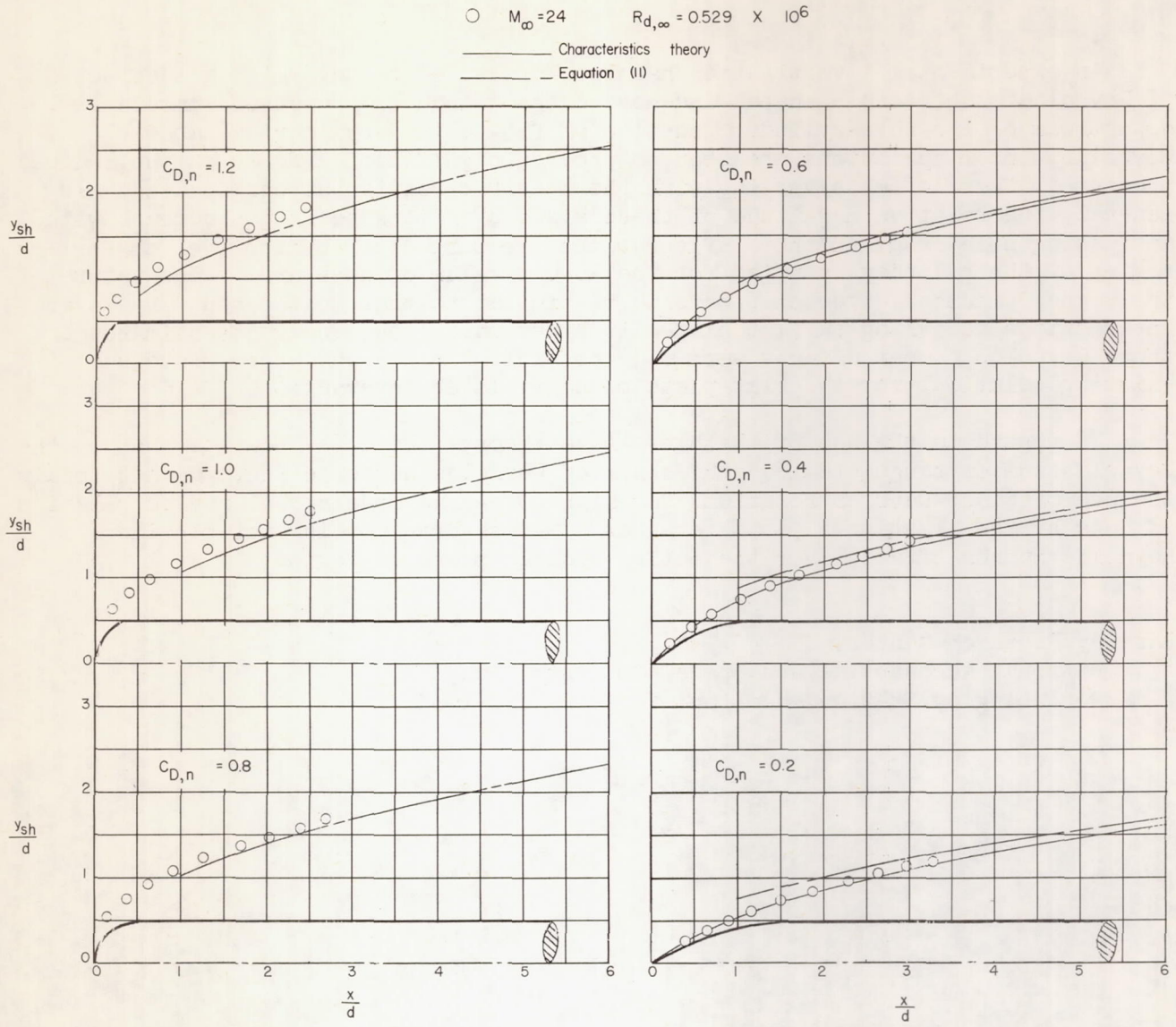

(b) Contoured-nose models.

Figure 12.- Concluded.

In regard to the nose-shape independence, a comparison of the shock coordinates (from the data and characteristics theory) between the cone and contoured-nose models reveals that beyond about 1 diameter from the nose-cylinder junction, the shocks are essentially independent of nose shape for a given value of $C_{D,n}$.

CONCLUDING REMARKS

An experimental investigation has been conducted to determine the effects of Reynolds number, nose shape, and nose drag on induced pressures immediately downstream of the nose-cylinder junction of flow-alined cylindrical models. Reynolds number variations are seen to produce significant effects on the induced pressures, these effects varying with the specific configurations studied. In general, the relative magnitude of these viscous effects tends to increase with decreasing nose drag and they influence the pressure distribution over the entire region of the cylinders studied for the lowest value of nose drag. The nature of the Reynolds number effects appears to be similar to that in the boundary-layer interactions occurring on flat plates in hypersonic flow, and good estimates of these Reynolds number effects were made possible through the appropriate use of existing solutions for the flat-plate boundary-layer interactions.

In regard to the use of the blast-wave theory, the data indicate that in the Reynolds number range studied, the observed Reynolds number effects do not impair the use of blast-wave correlations for high-nose-drag models, but any correlation of data by the blast-wave parameters for low-nose-drag models must consider Reynolds number effects over the entire induced-pressure region.

Langley Research Center,
National Aeronautics and Space Administration,
Langley Station, Hampton, Va., May 22, 1963.

APPENDIX

BOUNDARY-LAYER CALCULATIONS FOR CONTOURED-NOSE BODIES OF REVOLUTION

In order to determine whether the assumption of a boundary-layer growth effectively originating at the nose-cylinder junction of the slender contoured shapes was reasonable, the boundary-layer displacement thickness was calculated for two bodies of this type. The nose shapes for the bodies chosen were the contoured parabolic profile having $C_{D,n} = 0.2$ and a hemisphere capped by a 46° half-angle cone with $C_{D,n} = 0.8$. Characteristics solutions for both bodies gave the inviscid pressure distribution necessary for a solution in which local similarity was assumed. The general method outlined in reference 14 was followed in calculating the boundary layer.

Shown in figure 13 are the calculated boundary-layer displacement thicknesses for the nose-shoulder region of interest along with the inviscid pressures in this region obtained by the method of characteristics. It is evident from this figure that the boundary layer over the nose of the model is small in comparison with that downstream of the shoulder. Moreover, the shape of the boundary

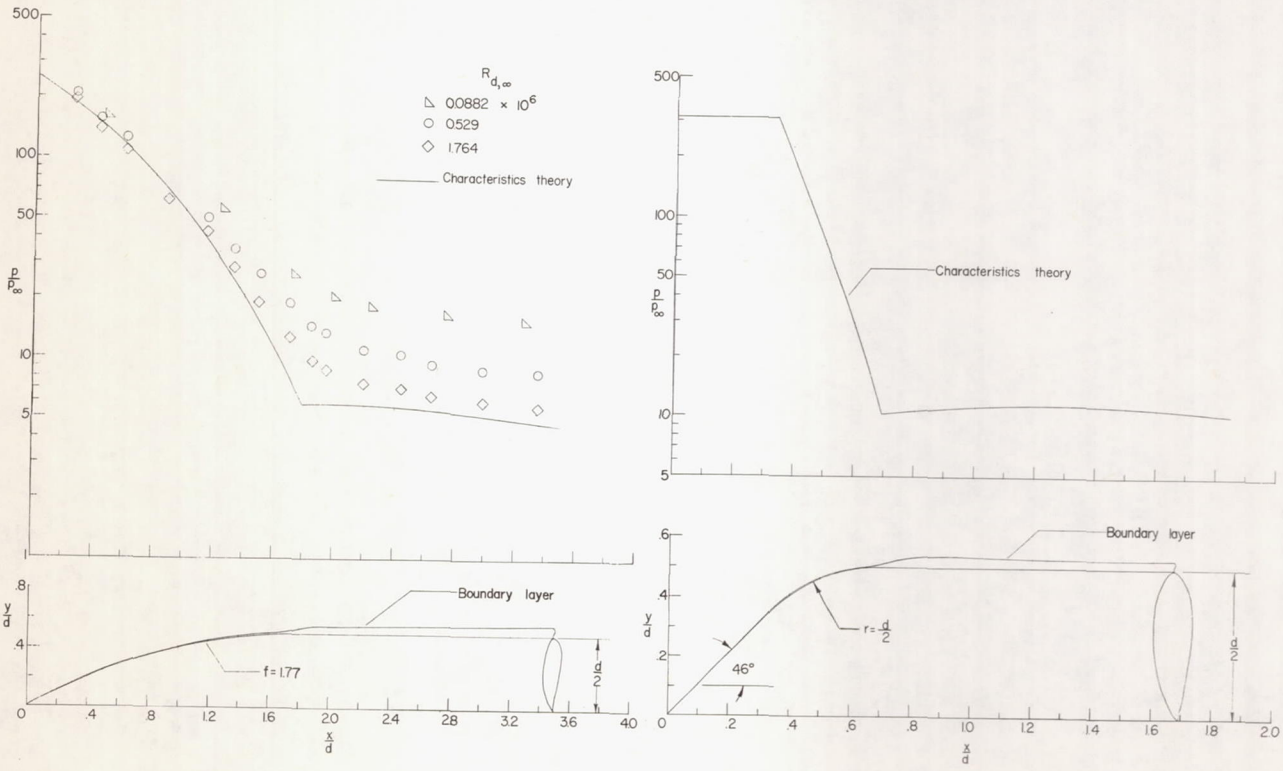

(a) $C_{D,n} = 0.2$; $R_{d,\infty} = 0.526 \times 10^6$; $M_\infty = 24$. (b) $C_{D,n} = 0.8$; $R_{d,\infty} = 0.0808 \times 10^6$; $M_\infty = 18$.

Figure 13.- Boundary-layer growth over axisymmetric bodies.

layer on the nose closely conforms to the model shape so that its presence should cause the pressure distribution to differ only slightly from the inviscid pressure distribution.

In view of the rapid rate of growth of the boundary layer in the shoulder region compared with that on the nose, the assumption of an effective origin of the boundary layer at the shoulder of the model would seem reasonable, even for low-drag contoured shapes.

As a matter of interest, the experimental data, shown in figure 13(a) for the contoured-nose model at several different Reynolds numbers, demonstrate the effect of boundary-layer growth on the pressure distribution.

REFERENCES

1. Cheng, H. K., and Pallone, A. J.: Inviscid Leading-Edge Effect in Hypersonic Flow. Jour. Aero. Sci. (Readers' Forum), vol. 23, no. 7, July 1956, pp. 700-702.

2. Mueller, James N., Close, William H., and Henderson, Arthur, Jr.: An Investigation of Induced-Pressure Phenomena on Axially Symmetric, Flow-Alined, Cylindrical Models Equipped With Different Nose Shapes at Free-Stream Mach Numbers From 15.6 to 21 in Helium. NASA TN D-373, 1960.

3. Witcofski, Robert D., and Henderson, Arthur, Jr.: Induced Pressures on Cylindrical Rods With Various Nose Drags and Nose Shapes at Mach Numbers of 17 and 21. NASA TN D-1266, 1962.

4. Bertram, Mitchel H., and Henderson, Arthur, Jr.: Recent Hypersonic Studies of Wings and Bodies. ARS Journal, vol. 31, no. 8, Aug. 1961, pp. 1129-1139.

5. Henderson, Arthur, Jr., and Baradell, Donald L.: Recent Work at Langley Research Center in the Development of Hypersonic Helium Tunnels. Proc. Nat. Symposium on Hypervelocity Techniques, Inst. Aero. Sci., Oct. 1960, pp. 131-141.

6. Van Hise, Vernon: Analytic Study of Induced Pressure on Long Bodies of Revolution With Varying Nose Bluntness at Hypersonic Speeds. NASA TR R-78, 1961.

7. Johnston, Patrick J., and Snyder, Curtis D.: Static Longitudinal Stability and Performance of Several Ballistic Spacecraft Configurations in Helium at a Mach Number of 24.5. NASA TN D-1379, 1962.

8. Erickson, Wayne D.: Real-Gas Correction Factors for Hypersonic Flow Parameters in Helium. NASA TN D-462, 1960.

9. Ferri, Antonio: Elements of Aerodynamics of Supersonic Flows. The Macmillan Co., 1949.

10. Love, E. S.: Generalized-Newtonian Theory. Jour. Aero/Space Sci. (Readers' Forum), vol. 26, no. 5, May 1959, pp. 314-315.

11. Bertram, Mitchel H., and Blackstock, Thomas A.: Some Simple Solutions to the Problem of Predicting Boundary-Layer Self-Induced Pressures. NASA TN D-798, 1961.

12. Lukasiewicz, J.: Hypersonic Flow-Blast Analogy. AEDC-TR-61-4 (Contract No. AF 40(600)-800 S/A 11(60-110)), Arnold Eng. Dev. Center, June 1961.

13. Hill, J. A. F., Baron, J. R., Schindel, L. H., and Markham, J. R.: Mach Number Measurements in High-Speed Wind Tunnels. AGARDograph 22, North Atlantic Treaty Organization (Paris), Oct. 1956.

14. Hayes, Wallace D., and Probstein, Ronald F.: Hypersonic Flow Theory. Academic Press, Inc. (New York), 1959.

NASA-Langley, 1963 L-3219